Article

Current Biology

Deterministic and Stochastic Rules of Branching Govern Dendrite Morphogenesis of Sensory Neurons

Graphical Abstract

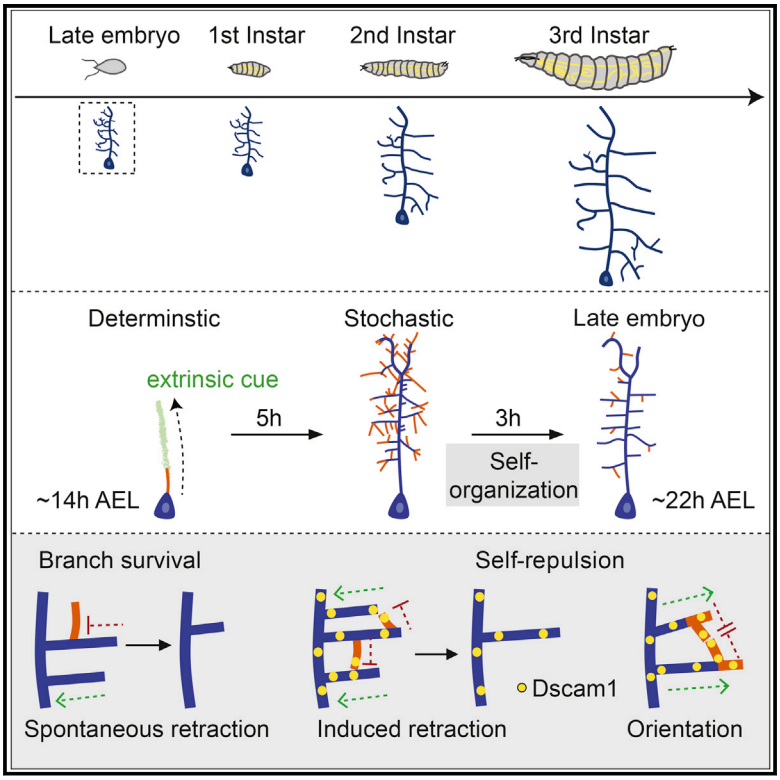

Authors

Amrutha Palavalli,
Nicolás Tizón-Escamilla,
Jean-François Rupprecht,
Thomas Lecuit

Correspondence

jean-francois.rupprecht@cpt.univ-mrs.fr (J.-F.R.),
thomas.lecuit@univ-amu.fr (T.L.)

In Brief

Palavalli et al. quantitatively detail vpda neuron morphogenesis and find that primary branches grow deterministically but secondary branches are stochastic. They develop a model for stochastic branching that reveals feedbacks of tree geometry on branch survival and show that self-repulsion patterns secondary branches by restricting direction of growth.

Highlights

- Core vpda neuron morphology is established during embryogenesis
- The primary branch grows deterministically but secondary branches are stochastic
- Tree architecture can increase or decrease the local probability of branch survival
- Contact-induced retraction selects secondary branches perpendicular to the primary

Palavalli et al., 2021, Current Biology *31*, 1–14
February 8, 2021
https://doi.org/10.1016/j.cub.2020.10.054

CellPress

Current Biology

CellPress
OPEN ACCESS

Article

Deterministic and Stochastic Rules of Branching Govern Dendrite Morphogenesis of Sensory Neurons

Amrutha Palavalli,[1] Nicolás Tizón-Escamilla,[2] Jean-François Rupprecht,[2,*] and Thomas Lecuit[1,3,4,*]

[1]Aix Marseille Université and CNRS, IBDM - UMR7288 and Turing Centre for Living Systems Campus de Luminy Case 907, Marseille 13288, France

[2]Aix-Marseille Université, Université de Toulon, CNRS, CPT, Turing Centre for Living Systems Campus de Luminy Case 907, Marseille 13288, France

[3]Collège de France, 11 Place Marcelin Berthelot, Paris 75005, France

[4]Lead Contact

*Correspondence: jean-francois.rupprecht@cpt.univ-mrs.fr (J.-F.R.), thomas.lecuit@univ-amu.fr (T.L.)

https://doi.org/10.1016/j.cub.2020.10.054

SUMMARY

Dendrite morphology is necessary for the correct integration of inputs that neurons receive. The branching mechanisms allowing neurons to acquire their type-specific morphology remain unclear. Classically, axon and dendrite patterns were shown to be guided by molecules, providing deterministic cues. However, the extent to which deterministic and stochastic mechanisms, based upon purely statistical bias, contribute to the emergence of dendrite shape is largely unknown. We address this issue using the *Drosophila* class I vpda multi-dendritic neurons. Detailed quantitative analysis of vpda dendrite morphogenesis indicates that the primary branch grows very robustly in a fixed direction, though secondary branch numbers and lengths showed fluctuations characteristic of stochastic systems. Live-tracking dendrites and computational modeling revealed how neuron shape emerges from few local statistical parameters of branch dynamics. We report key opposing aspects of how tree architecture feedbacks on the local probability of branch shrinkage. Child branches promote stabilization of parent branches, although self-repulsion promotes shrinkage. Finally, we show that self-repulsion, mediated by the adhesion molecule Dscam1, indirectly patterns the growth of secondary branches by spatially restricting their direction of stable growth perpendicular to the primary branch. Thus, the stochastic nature of secondary branch dynamics and the existence of geometric feedback emphasize the importance of self-organization in neuronal dendrite morphogenesis.

INTRODUCTION

Dendrites are neuronal processes specialized to receive information. Neuronal subtypes have strikingly different dendrite arborization patterns. These patterns depend on several factors, like the number and types of synaptic or sensory inputs received by the neuron or the geometry and size of the receptive fields. Failure to establish proper branching patterns leads to various neurodevelopmental disorders.[1]

In general, dendrite morphogenesis follows a set of consecutive steps, which include (1) dendrite initiation, (2) outgrowth, (3) branching and maturation, and (4) establishment of boundaries and, sometimes, arbor remodeling.[2,3] Every step requires extensive regulation by cell intrinsic as well as extrinsic cues.

Dendrite morphology is regulated cell-intrinsically by transcription factors,[4–8] cytoskeletal regulators,[9–15] components of endocytic pathway,[16–18] and secretory pathway,[19,20] all of which have been shown to either promote or reduce dendrite branching.

Extrinsic cues include long-range diffusible secreted factors that are classically involved in axon guidance, like semaphorins,[21] slits,[22–24] and netrins,[25–27] which promote or restrict dendrite branching. Contact-mediated, short-range cues, like cell adhesion molecules and adhesion GPCRs, guide branch points,[28] restrict branching,[29] and maintain dendrites in a 2D plane.[30] Neuronal activity also refines arbor morphology by increasing or decreasing branching density.[31,32] Though much is known about the molecules regulating dendrite branching, how they govern the neuron-specific arborization patterns remains unclear. Indeed, most molecules tend to increase or decrease branching density without significantly affecting arborization patterns.

Two modes of branching morphogenesis have emerged from studying other branched organ systems.[33–35] The first is deterministic, where systems have highly stereotyped branching patterns as described in the mouse lung[36] and *Drosophila* tracheal system.[37] Branching is orchestrated by patterned cues, such as *Drosophila* fibroblast growth factor (FGF), which is expressed in clusters of cells surrounding the tracheal sacs at specific positions and instructs the branch points of the primary bud.[37] The dendrites of the *C. elegans* PVD neuron represent an extreme example of deterministic patterning in the neuronal system. The branch points in the complex menorah-like PVD dendrites are almost exclusively determined by patterned cues in the epidermis.[28,38–40] The second mode of branching is self-organized, wherein final morphology emerges from statistical

Please cite this article in press as: Palavalli et al., Deterministic and Stochastic Rules of Branching Govern Dendrite Morphogenesis of Sensory Neurons, Current Biology (2020), https://doi.org/10.1016/j.cub.2020.10.054

features of branch dynamics and local interactions between growing tips. This results in stochastic branch patterns as described in mammary glands.[34] Although extrinsically derived FGF promotes branching in this system, no patterned cue has been identified that could potentially guide branching.[41,42] Mammary gland branching can be fully recapitulated by a model that accounts for local parameters, such as tip elongation rate, branching rate, and mode of tip termination.[34] Thus, branching morphogenesis of the mammary gland follows a stochastic, self-organized scheme and does not seem to require extrinsically patterned cues.

In neuronal systems, cell fate has traditionally been thought to be achieved deterministically by specific regulatory genes,[43,44] but neuronal connectivity is refined by an activity-dependent, self-organization.[45] Although overall shapes of homologous neurons are constant, their finer details are not.[46,47] Thus, we wanted to further investigate the relative contribution of deterministic and self-organized mechanisms in establishing dendrite patterns.

The *Drosophila melanogaster* multi-dendritic-dendritic arborization (md-da) neurons are the model of choice to address this question. Md-da neurons are part of the peripheral nervous system and are involved in somatosensation. They are divided into four distinct morphological classes in an increasing order of dendritic complexity. They exhibit stereotyped dendritic structures identifiable across animals and are restricted in a 2D space beneath the epidermis.[48–51] Md-da neurons have been extensively used to study dendrite morphogenesis, especially class I and class IV neurons, which exhibit the simplest and most complex morphologies, respectively.[6,8,52,53] However, most studies are based on fixed imaging and have focused on late developmental stages, after the establishment of the typical dendritic morphology of the four neuronal classes.

In this study, we use high-resolution live imaging to quantitatively describe morphogenesis of class I vpda neurons. We show that the primary dendrites grow deterministically although secondary dendrite patterning is stochastic. Additionally, our computational model and Dscam1 data show that self-repulsion patterns secondary dendrites by preferentially stabilizing them orthogonally from the primary dendrite, giving the class I neurons their characteristic morphology.

RESULTS

Class I vpda Neuron Shape Is Established during Embryogenesis

To understand how class I-specific dendrite morphology is achieved, we first investigated when final morphology of the dendritic arbor is established. The vpda neuron has one large primary dendrite that projects dorsally and a small primary branch on the ventral side. Secondary dendrites project outward from the side of the primary dendrites, giving vpda neurons their characteristic ''bottle brush'' morphology.

Dendrite morphology was analyzed at 4 developmental stages, i.e., late embryogenesis (embryonic stage 17 [E17], 19 ± 2 h after egg laying [AEL]), first instar (L1, 24 ± 3 h AEL), second instar (L2, 48 ± 3 h AEL), and third instar (L3, 72 ± 3 h AEL). Neurons were labeled with upstream activating sequence (UAS)-mCD8::GFP, expressed by the neuronal class-I-specific driver 2-21 gal4.[5] We observed a qualitative enlargement of the neurons that correlated with growth of the organism (Figure 1A). To confirm this, we developed tools to quantitatively describe dendrite morphology. vpda neuron dendrites were segmented and classified into primary, secondary, tertiary, and quaternary branches (schematic Figures 1A and S1A–S1C). The branch numbers for each order of complexity were first measured. On average, 15–17 secondary branches emerged from the primary branch across the four developmental time points, showing no statistically significant changes during development (Figure 1B). The primary and secondary branches made up the bulk of the total dendrite length (84.6% on average) at L3. The tertiary and quaternary branches made up, on average, 15.4% of the total dendrite length at L3 (Figure S1D) and varied somewhat during development, but this did not significantly alter the global dendrite pattern.

The total dendrite lengths made up by the primary, secondary, tertiary, and quaternary branches also did not vary greatly across all 4 developmental stages (Figure S1D). Thus, the core morphology of vpda neurons dendrites is established in the embryo. Consistent with this, the relative distance between secondary branches did not change over time (Figure 1C), confirming that the dendrite pattern scales isometrically in size as the larva grows.

Thus, we set out to image dendrite morphogenesis in living embryos. Using a novel imaging setup, we obtained movies covering complete dendrite morphogenesis (Video S1). These movies reveal 3 phases in vpda neuron morphogenesis: (1) primary dendrite formation: between 13 and 15 h AEL, vpda neurons extend a single and stable primary dendrite toward the dorsal region of the embryo (Video S2). (2) Secondary branch initiation and elongation: after ~15 h AEL, flat lamellipodia-like membrane protrusions appeared at the distal tip of the primary dendrite (Figure 1D, i and ii). At ~17 h AEL, numerous, small, and dynamic protrusions that constantly extended and retracted appeared everywhere along the primary dendrite (Figure 1D, iii). These dynamic protrusions were termed secondary extensions to distinguish them from stable secondary branches observed at later stages. On average, 28.2 ± 6.4 secondary extensions were present at 17 h AEL (Figure 1E). Over the next 3 to 4 h, these extensions elongated at a rate of ~1 μm/h (Figure 1F). The growth of secondary extensions was accompanied by the emergence of dynamic protrusions branching off from secondary extensions, termed tertiary extensions. (3) Secondary branch stabilization: after 20 h AEL, the dendritic structure became markedly less dynamic and secondary extension lengths (6 ± 1.2 μm) and numbers (17.6 ± 3) stabilized at 22 h AEL (Figures 1E and 1F). On average, 62.3% of the initial secondary extensions were stabilized as secondary dendrites (Figure 1E). The number of tertiary extensions dropped as the secondary extensions stabilized into secondary dendrites (Figures 1F and 1G). This number is even lower at later L1 (Figure 1B). Unlike secondary extensions, no drastic change in tertiary extension lengths was observed over time (Figure 1H).

In summary, the primary branch grows dorsally in a straightforward manner followed by the emergence of dynamic secondary extensions undergoing repeated cycles of extension and retraction until stabilization of a subset of branches. Our observations reveal striking differences in the mode of development of the primary and secondary dendrites.

Please cite this article in press as: Palavalli et al., Deterministic and Stochastic Rules of Branching Govern Dendrite Morphogenesis of Sensory Neurons, Current Biology (2020), https://doi.org/10.1016/j.cub.2020.10.054

CellPress
OPEN ACCESS

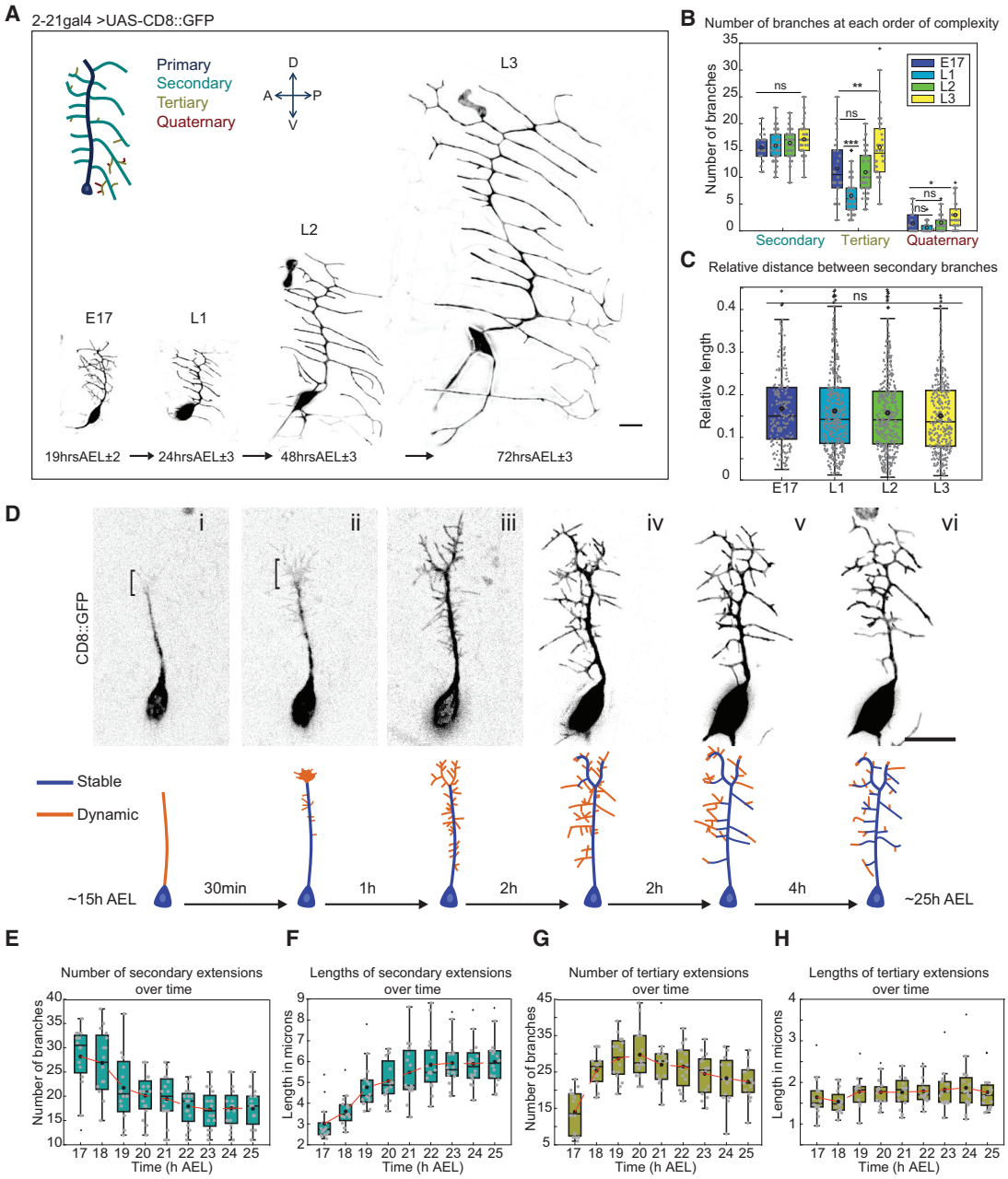

Figure 1. Class I vpda Neuron Shape Is Established during Embryogenesis

(A) vpda neurons from homozygous 2-21 gal4/UAS-mCD8::GFP at embryo (E17 19 h AEL ± 2), L1: 24 h AEL ± 3, L2: 48 h AEL ± 3, and L3: 72 h AEL ± 3. Schematic: primary branch (blue); secondary branches (cyan); tertiary (brown); quaternary (red).

(B) Number of branches at each order of complexity. E17 n = 26, L1 n = 48, L2 n = 50, and L3 n = 38 neurons.

(C) Relative distance (inter-dendrite distance/primary branch length). E17 n = 194, L1 n = 374, L2 n = 409, and L3 n = 341 segments.

(D) Top panel: dendrite development in *mhc*1 mutant background embryos (Video S1). Lower panel: scheme of dendrite development is shown. Blue, stable dendrites; orange, dynamic extensions.

(E–H) Numbers and lengths of (E and F) secondary and (G and H) tertiary branches over ~17 to ~25 h AEL; n = 16 neurons. For each box, central line is median, "o" is the mean, the box extends vertically between the 25th and 75th percentiles, the whiskers extend to the most extreme data not considered outliers, and outliers are plotted individually.

Statistical significance calculated using Mann-Whitney U test for (B) and (C). ns, not significant; *p < 0.05; **p < 0.01; ***p < 0.001. All the panels have the same orientation; dorsal: top, anterior: left. Scale bars represent 10 μm. See also Figure S1 and Video S1.

Please cite this article in press as: Palavalli et al., Deterministic and Stochastic Rules of Branching Govern Dendrite Morphogenesis of Sensory Neurons, Current Biology (2020), https://doi.org/10.1016/j.cub.2020.10.054

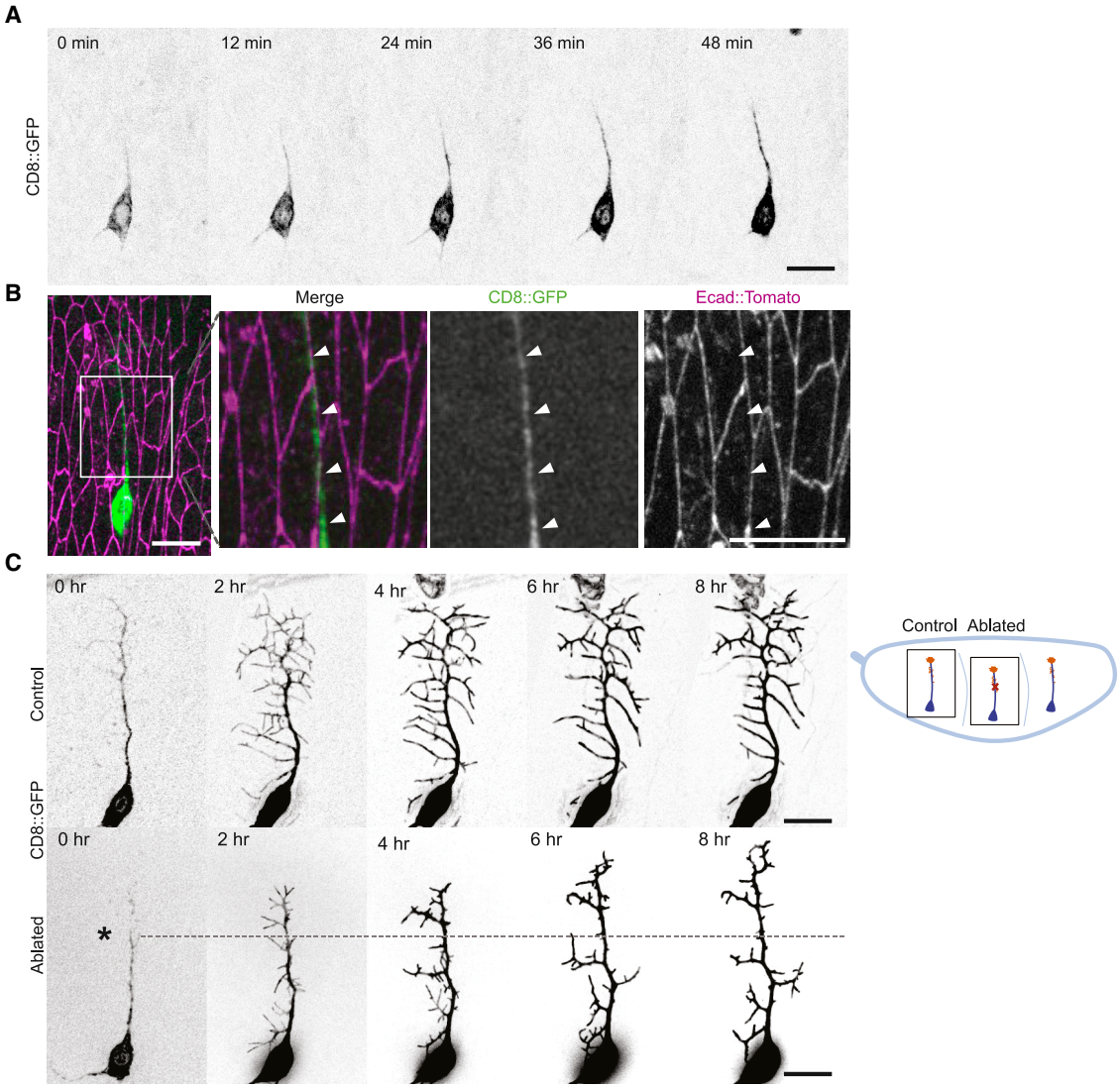

Figure 2. Growth of the Primary Dendrites Is Deterministic

(A) Primary dendrite development of homozygous 2-21 gal4/UAS-mCD8::GFP, *mhc*1 embryos (Video S2).

(B) Neuron at ~15 h AEL co-imaged with Ecad::tomato. Inset: close up of primary dendrite following E-cadherin cell boundaries indicated by white arrowheads is shown.

(C) Schematic: control and ablated neurons from the same embryo. Red X: ablation site. Control (top panel) and ablated neuron (bottom panel; Video S3) are shown. Dashed line: point of ablation.

Scale bars represent 10 μm. See also Figure S2 and Videos S2 and S3.

Growth of the Primary Dendrites Is Deterministic

vpda neurons consistently form single dorsal primary dendrites that extend toward the dorsal region of the embryo (Figure 2A; Video S2). This reproducible growth pattern suggested a stringent control of primary dendrite number and orientation and hence deterministic growth.

When E-cadherin was co-expressed with the neurons to label the overlying epithelial cells, the primary dendrite coincided with the cadherin signal in 70% of the cases (17/24; Figure 2B). Interestingly, even when the primary dendrite did not coincide with cadherin signal, it tracked parallel to these cell boundaries (Figure S2A). This hinted at the presence of a cue guiding the primary dendrite.

To assess the robustness of primary dendrite development, we mechanically perturbed growth by focusing an infrared laser to a point on the primary dendrite to cut a part of it at ~16 h AEL and subsequently observed its recovery. We hypothesized that the dendrite would not be able to continue growing dorsally as the guidance cue may be lost, because the ablation was carried out at a time after the completion of primary dendrite development. However, in all examined cases (n = 15), ablated primary dendrites recovered and continued to grow dorsally (Figure 2C; Video S3). This suggested that a persistent cue guided the primary dendrite. Together, these observations support the idea that primary dendrite number and orientation are defined deterministically.

Morphogenesis of the Secondary Dendrites Is Stochastic

Secondary branch growth was much more dynamic than primary branch growth (Figure 1). We also observed a higher variation in numbers of secondary branches. These observations argued against strictly deterministic growth. We therefore further investigated secondary dendrite growth properties.

At L3, secondary branch numbers ranged from 10 to 25 per neuron (mean 17 ± 3; Figure 1B). This is consistent with stochastic systems where branching features are variable but distributed around a peak when analyzed statistically. However, this variation could reflect intersegment variability as neurons from all the abdominal hemi-segments were analyzed. Thus, we pooled data from larval dendrites of the same abdominal segment (A3; Figure 3A). Secondary branch numbers ranged from 11 to 24 with a peak at 18 ± 2.6 (Figure 3B), similar to Figure 1B.

However, this observed variation could also be an outcome of age variability between larvae. Hence, we compared dendrites from the left and right A3 hemi-segment of the same larva. The difference in secondary branch number between the left-right pairs (Figure 3C) ranged from −7 to 7 with a mean difference of −1 ± 3.6 between the pairs, indicating a high variability of branch number. Thus, secondary branch numbers are not tightly controlled but rather a result of stochastic differences arising during morphogenesis.

Interestingly, the variability of secondary branches between A2 and A3 segments on the left had similar distributions to left-right differences (Figures S2B–S2D), further supporting that intersegment variation is mainly due to stochastic processes.

Further, we measured primary and secondary branch lengths at ~24 h AEL. Primary branch lengths varied by 10.6% of the mean (Figure 3D), although for secondary branches, variability was 57.7% (Figure 3E), further supporting the idea that primary branch growth is deterministic although secondary branch development is stochastic.

We then imaged growth at a higher temporal resolution (every 30 s; Video S4). In contrast to the unidirectional growth of primary dendrites (Figure 2A), secondary and tertiary extensions alternated between phases of extension and retraction and, in doing so, frequently changed direction (Figures 3F, i, and 3G–3I). Further, secondary and tertiary extensions retracted upon contact with neighboring extensions (Figure 3F, ii) or self-repulsed. Growth rates of the secondary extensions also progressively reduced with time, particularly between 17 and 20 h AEL (Figure 3J).

In summary, secondary branch numbers arose stochastically from an initial higher number of dynamic extensions that self-repulse. This led us to explore how reproducible branching patterns emerge from the stochastic branch dynamics using a computational model.

A Computational Model of Dendrite Branching

Typical class I morphology is characterized by lower branch densities (total dendrite length per unit area is 0.0104/μm) and smaller dendritic fields compared to other morphological classes, such as class IV neurons (0.07/μm).[54] To identify key mechanisms responsible for dendrite patterning, we developed a computational model for stochastic branching to simulate secondary dendrite morphogenesis.

In our 2D model (Figure 4A), extensions were modeled as polymers that grow (extend) and shrink (retract). We began with a fully formed primary dendrite (length $L_1 = 30\mu m$), which remained unaltered during the simulation. This corresponded to the neuron at ~15 h AEL *in vivo*. New secondary extensions branch from the side of the primary dendrite at a rate λ_1. At simulation time $t = 16$ h AEL, tertiary (respectively [resp.] quaternary) extensions emerge from the sides of pre-existing secondary (resp. tertiary) extensions at rates λ_2 (resp. λ_3). Once an extension appears, it either polymerizes (i.e., grows) or depolymerizes (i.e., shrinks) with growth or shrink velocities $v_{(2,3,4),on}$ and $v_{(2,3,4),off}$, where the subscript number represents the order of complexity of the extension, with persistence length l_p. An extension can spontaneously switch from a polymerizing to depolymerizing state (or vice versa) with a rate k_{off} (or k_{on}, respectively). To complete the model, we introduced a contact-induced depolymerization or "self-repulsion" as observed *in vivo* (Figure 3F, ii). When a polymerizing extension encounters a neighboring dendrite, it stops and shrinks with a probability p_{off}. Unless otherwise stated, we set $p_{off} = 1$, implying that extensions will always retract upon contact with neighbors.

We explored constitutive parameters of the model and found that a range of different dendrite morphologies can be described using this computational scheme. Branching rate (λ), growth rate (v), and the ratio of spontaneous switching rates, $r = k_{on}/k_{off}$, played a fundamental role in dendrite architecture. Higher growth rates resulted in dendrites with larger dendritic field areas and longer branches (Figure 4C). On the other hand, increasing branching rates increased branch numbers (Figures S3A and S3D). The ratio of spontaneous switching rates r had the highest impact on neuron morphology. For any value of both branching and growth rates, we could account for the wide phenomenology described by this model by simply changing the value of r. For low r values (i.e., higher probability of switching to a depolymerizing state), only a few short secondary extensions survived to final stages. For intermediate r values, moderate branch densities emerged, similar to class I dendrites. Finally, for values of r close or equal to 1, we obtained dendrites with very high densities and very large total areas (Figure 4C). This qualitative trend was observed irrespective of both growth and branching rates (Figures 4C, S3A, and S3B).

However, despite an extensive parameter exploration, we were unable to find quantitative agreements between *in vivo* and simulated branches; the time evolution of branch number in simulated dendrites consistently deviated from *in vivo* values (Figures S3C, S3D, 4E, and 4F, blue lines). Considering that *in vivo*, secondary branch dynamics slows down over time (Figures 3G–3J), we incorporated a progressive decay of all dynamic parameters or an "aging factor." We reduced the rates of growth, branching, and switching over time with differing intensities. We obtained arborization patterns that ranged from being barely affected with highly active dendrites (for small aging factors) to dendrites that nearly froze at early stages exhibiting low-density arborization patterns (for high aging factors). Additionally, larger switching ratios required more-intense aging factors in order to obtain branch numbers and lengths consistent with *in vivo* observations at intermediate and final stages (Figure S3E). To explore this, we chose two parameter sets with switching ratios $r = 0.75$ and $r = 1$ and applied two aging protocols, AP1 and AP2, respectively (Figure 4D; Table 1 Option 1

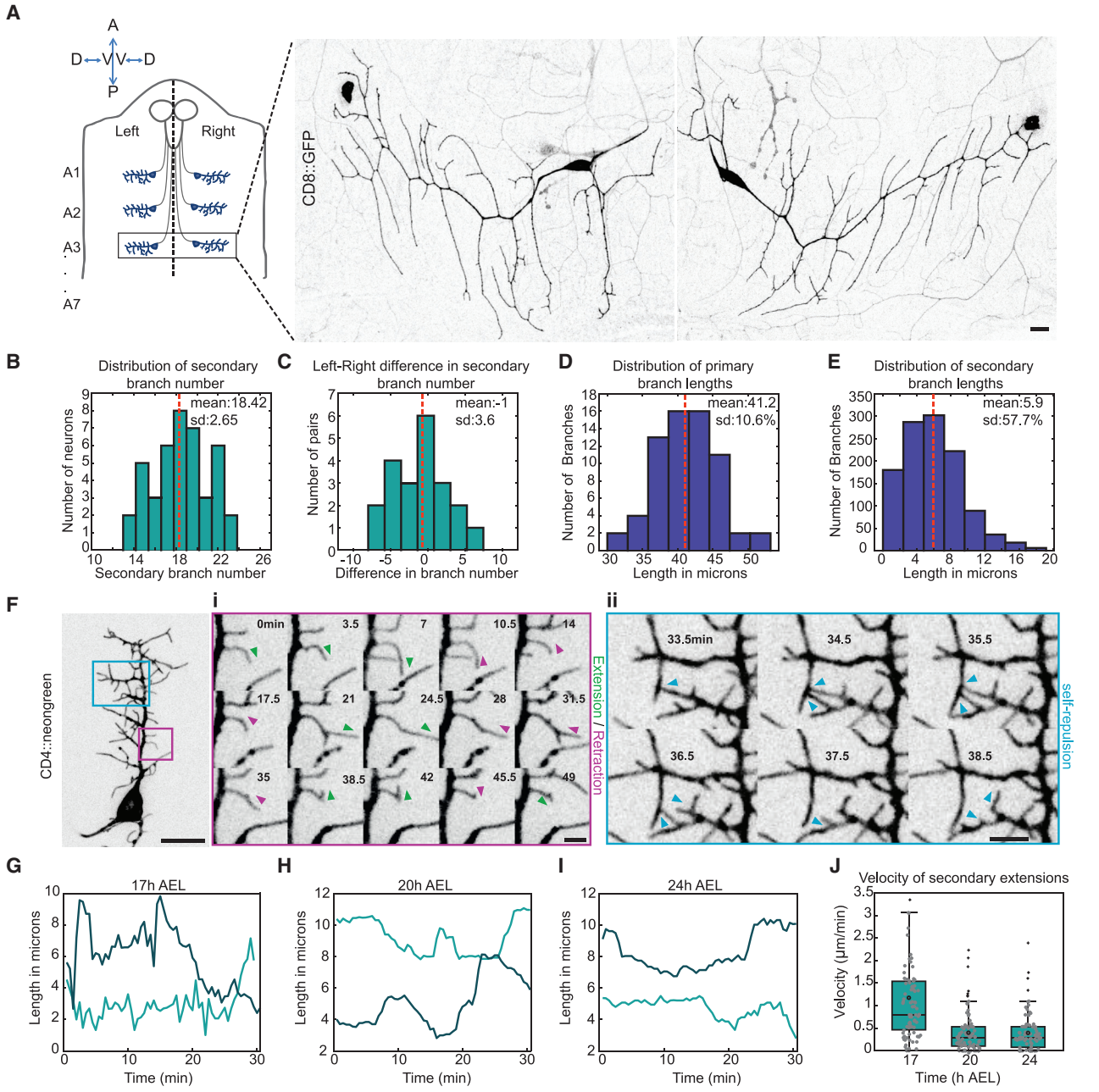

Figure 3. The Development of the Secondary Dendrites Is Stochastic

(A) Schematic: larval filet; vpda neurons in abdominal hemi-segments. A3, left and right vpda neurons at 96 h AEL ± 3 from homozygous 2-21 gal4/UAS-mCD8::GFP. Panel orientation; anterior: top, posterior: bottom, ventral: center and dorsal to the sides.

(B) Distribution of secondary branch number.

(C) Distribution of difference in secondary branch number between left-right pairs. For (B) and (C), n = 42 neurons (21 left-right pairs).

(D and E) Distribution of (D) primary (n = 66 branches) and (E) secondary branch lengths. At 22 h AEL ± 2, n = 1,140 branches (n = 66 neurons).

(F) Time-lapse of secondary branch development (~18 h AEL; Video S4). (i) Green arrowheads, extending dendrite; magenta arrowheads, retracting dendrite. (ii) Blue arrowheads indicate self-repulsion. Panel orientation: dorsal at the top, anterior to the left.

(G–I) Secondary extension lengths over time. Trend lines indicate two individual branches.

(J) Velocities of secondary extensions.

Scale bars represent 10 µm. See also Figure S2 and Video S4.

Please cite this article in press as: Palavalli et al., Deterministic and Stochastic Rules of Branching Govern Dendrite Morphogenesis of Sensory Neurons, Current Biology (2020), https://doi.org/10.1016/j.cub.2020.10.054

CellPress
OPEN ACCESS

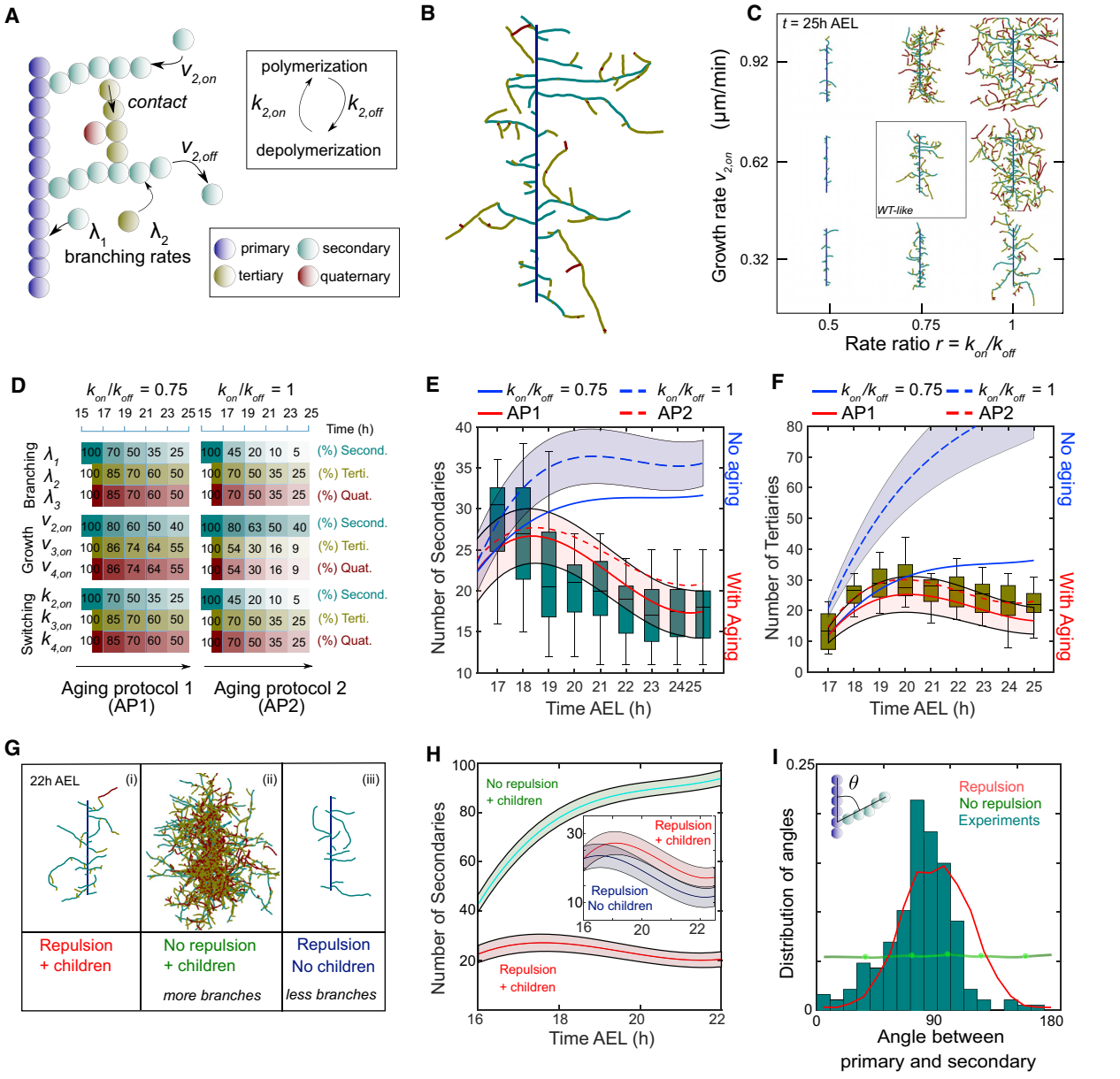

Figure 4. A Computational Model of Dendritic Branching and Feedback of Tree Architecture on Branch Stabilization and Orientation

(A) Scheme of the computational model.

(B) Simulated dendrite at 25 h AEL.

(C) Ratio of spontaneous switching rates $r = k_{on}/k_{off}$ versus growth rate $v_{2,on}$ (growth rates of tertiary and quaternary branches; $v_{3/4,on} = v_{2,on}/2$). Other parameters are in Table 1, option 1.

(D) Aging protocols AP1 $(r = 0.75)$ and AP2 $(r = 1)$. Parameters reduced every 2 h as indicated by parameter percent values.

(E and F) Number of (E) secondary and (F) tertiary branches over time. In (E) and (F), blue lines are simulations without aging, red lines are simulations with aging, and boxplots are experimental data.

(G) Dendrites at 22 h AEL for (i, red) self-repulsion with child branches; (ii, green) no self-repulsion, with child branches; and (iii, blue) self-repulsion without child branches.

(H) Number of secondary branches using AP1 for (G, i and ii). Inset: simulation for (G i and iii) is shown.

(I) Probability distribution of angles between primary and secondary branches (22 h AEL). Histograms represent *in vivo* data; red and green lines represent simulations with and without self-repulsion using AP1.

For (E) and (F), (blue lines) $N_{sim} = 50$. For red lines (E, F, H, and I), $N_{sim} = 500$. Simulation lines are average values, and shadows are 1σ confidence interval. A 2-point time averaging was performed using spline interpolation for lines in (E), (F), and (H). Initial computational parameters in AP1 (E–I) and AP2 (E and F) are in Table 1, options 1 and 2, respectively. See also Figure S3 and Video S5.

Please cite this article in press as: Palavalli et al., Deterministic and Stochastic Rules of Branching Govern Dendrite Morphogenesis of Sensory Neurons, Current Biology (2020), https://doi.org/10.1016/j.cub.2020.10.054

Table 1. Computational Parameters

Parameters		Notation	Option 1	Option 2
Time step (**min**)		Δt	0.5	0.5
Length primary branch (**μm**)		L_1	30	30
Number of beads in primary branch		N_1	100	100
Branching rate (μm^{-1} min^{-1})	secondary	λ_1	0.22	0.12
	tertiary	λ_2	0.05	0.05
	quaternary	λ_3	0.02	0.02
Growth/shrink rates (**μm** min^{-1})	secondary	$v_{2,on/off}$	0.62	0.32
	tertiary	$v_{3,on/off}$	0.31	0.18
	quaternary	$v_{4,on/off}$	0.31	0.18
Persistence length (**μm**)		l_p	17	17
Spontaneous switching rate to a polymerizing state (min^{-1})		k_{on}	0.5	0.67
Spontaneous switching rate to a depolymerizing state (min^{-1})		k_{off}	0.67	0.67

See also Figures 4 and S3.

and 2 respectively). The resulting branch numbers and lengths were consistent with *in vivo* observations for both protocols (Figures 4E, 4F, red lines, S3F, and S3G). Notably, for AP1, growth velocity was set to 0.62 μm/min, in accordance with *in vivo* measurements (Figure 3J; Video S5).

Thus, our computational model predicts the emergence of a range of possible dendrite morphologies from a few local statistical features of branch dynamics. For a wide subset of the parameter space, the combination of all the different elements of the model leads to arborization patterns consistent with *in vivo* observations.

Feedback of Tree Architecture on Secondary Branch Stabilization and Orientation

Although the dynamics of branches is partly governed by a few constitutive parameters that are homogeneous in space, simulations also revealed the importance of feedback of dendritic tree geometry on local branch dynamics.

The *in vivo* observation that a depolymerizing secondary extension (parent branch) does not shrink beyond the branching point of any existing tertiary extensions (child branches) was incorporated in the simulations (Figure S2D; Video S6). With this mechanism, child branches protect depolymerizing parent branches from complete shrinkage. When we prevented tertiary and quaternary extensions (child) from forming in simulations, fewer secondary branches (parent) were observed (Figures 4G, iii, and 4H, blue lines). Thus, child branches reduce the probability of complete branch elimination, giving rise to branch self-stabilization.

The most striking feature of secondary branch morphogenesis was self-repulsion, which occurred quite frequently, hinting at an important role in patterning. We thus decided to further explore this observation.

When a new extension emerges in a region surrounded by other extensions, its probability of survival strongly decreases, because its probability of encountering neighbors is high. Thus, branching density can feedback negatively on branch number. This in turn affects tertiary extensions, as they are more likely to encounter neighbors (Figure S3H, top). Our simulations with and without self-repulsion confirmed that self-repulsion strongly reduces secondary branch numbers (Figures 4G and 4H, red and green lines) and lengths (Figure S3H, bottom).

Self-repulsion also strikingly impacted dendrite orientation. The distribution of angles made by the secondary dendrites on the primary both in simulations and experiments peaked at around 90°. Lower-frequency values were observed around both 0° and 180°. Thus, secondary dendrites tend to be oriented orthogonally to the primary dendrite. When contact-induced depolymerization was eliminated, we observed a uniform angle distribution (Figure 4I). Hence, in our simulations, the observed orientation of secondary dendrites does not require a guidance cue per se but is an outcome of a branch-selection process that minimizes branch density and crossover through self-repulsion. Thus, self-repulsion is potentially a key feature responsible for the characteristic bottle brush shape of vpda neurons.

Thus, in our model, the dendritic tree geometry, which emerges from the local branch dynamics, exerts positive (self-stabilization by child branches) and negative feedbacks (branch elimination and shrinkage through self-repulsion) on branch dynamics by effectively changing the rate of shrinkage.

Dscam1 Restricts the Orientation of Secondary Dendrites

To further test our model, we investigated the impact of self-repulsion *in vivo* using *dscam1* mutants. Dscam1 is a type I membrane protein of the immunoglobulin superfamily[55] expresse d in all 4 neuronal classes, playing a role in cell identity. Its loss causes self-avoidance defects in all classes of md neurons.[56–58] All previous studies observed *dscam1* mutants at later stages, when dendrite patterning was complete. Thus, how self-avoidance affects the emergence of dendrite patterns remains unknown.

The embryonic development of vpda neurons was observed in $dscam^{P1}$ mutants[55,56] over a *dscam1* deletion line, marked with CD4::neon green. The mutant and control embryos were imaged from 17 to 22 h AEL (Figure 5A; Video S7). The development of the primary branch was unaffected in the mutant (Figure S4A), with no significant difference in the primary branch length measured at 22 h AEL (Figure S4B).

At 22 h AEL, $dscam^{P1}$ dendrites do not appear to share the high branching densities of simulations without self-repulsion

Please cite this article in press as: Palavalli et al., Deterministic and Stochastic Rules of Branching Govern Dendrite Morphogenesis of Sensory Neurons, Current Biology (2020), https://doi.org/10.1016/j.cub.2020.10.054

CellPress
OPEN ACCESS

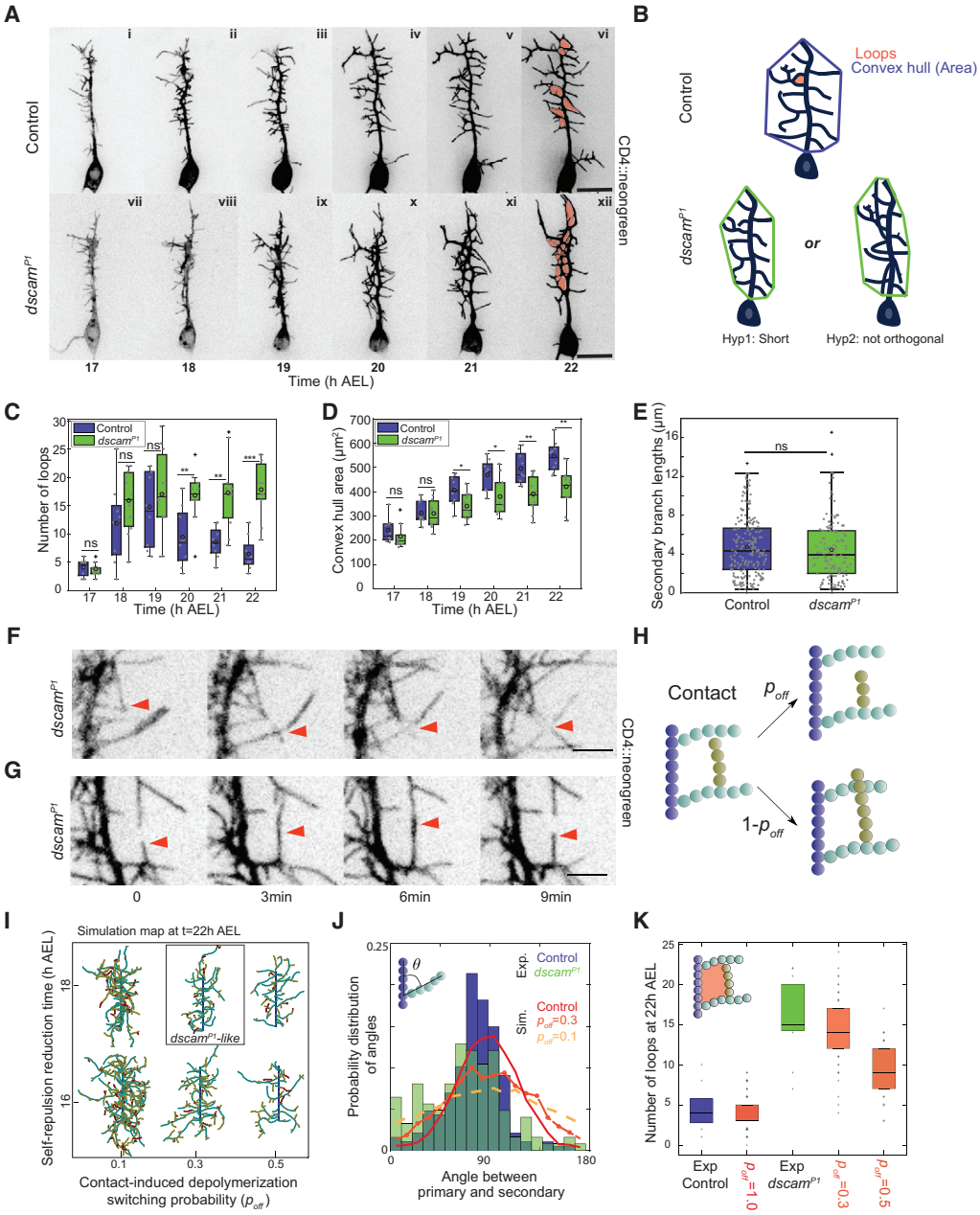

Figure 5. Dscam1 Restricts the Orientation of Secondary Dendrites

(A) Dendrite development of (top panel) homozygous 2-21 gal4/UAS-mCD4::neongreen and (lower panel) $dscam^{P1}$/ΔDscam1; 2-21 gal4/UAS-mCD4::neongreen neurons (Video S7).

(B) (Top panel) Area of the convex hull (control). Red shadow, loops formed by dendrite crossovers. (Bottom panel) $dscam^{P1}$ dendrites are (i) shorter or (ii) not orthogonal.

(C) Number of loops.

(D) Dendritic field area.

For (C) and (D), control (blue) n = 9 and mutant (green) n = 11 neurons.

(E) Secondary branch lengths. Control n = 206; mutant n = 142 branches.

(F) Loss of repulsion: red arrows show dendrite crossover.

(G) Self-repulsion: red arrows show remnant self-repulsion $dscam^{P1}$ (Video S8).

(H) Upon contact with a neighbor, extensions either cross over neighbors with probability $1-p_{off}$ or switch to depolymerizing states with probability p_{off}.

(I) Dendrite morphologies at 22 h AEL for different values of p_{off} introduced at different time points.

(legend continued on next page)

Please cite this article in press as: Palavalli et al., Deterministic and Stochastic Rules of Branching Govern Dendrite Morphogenesis of Sensory Neurons, Current Biology (2020), https://doi.org/10.1016/j.cub.2020.10.054

(Figure 4G, ii). We thus carefully examined morphogenesis of *dscam1* mutants to understand how it is different from simulations without repulsion.

Consistent with previous studies performed at later stages, at 22 h AEL, mutant dendrites frequently crossed over each other, thereby forming apparent "loops" in the dendrite architecture (Figures 5A, xii, and 5B). These loops were also observed to a lesser extent in control dendrites (Figure 5A, vi). The number of loops increased in both control and mutant embryos from 17 to 19 h AEL. However, from 20 to 22 h AEL, the number dropped strongly in controls but was maintained in mutants (Figure 5C). This meant that, from 17 to 19 h AEL, the secondary and tertiary extensions explore the space around them and contact their neighbors in both genetic conditions. However, over time, these contacts are not maintained in control embryos due to self-repulsion but persist in the *dscam1* mutant.

Additionally, the dendritic field area (Figure 5B) covered by the dendrite was smaller in mutants than in controls. The area of the dendrites became significantly smaller in *dscam1* mutants from 19 h AEL and was on average 20% smaller at 22 h AEL (Figure 5D). The smaller dendritic field areas of $dscam^{P1}$ meant that the secondary branches are either shorter (Figure 5B, Hyp1) or that they are not perpendicular to the primary branch (Figure 5B, Hyp2), as seen in simulations without self-repulsion (Figure 4I). To test these hypotheses, we measured secondary branch lengths at 22 h AEL and found no significant difference between mutants and controls (Figure 5E). This suggested that the reduced dendritic field is due to a loss of secondary branches that are oriented perpendicular to the primary branch. We measured a significant reduction in the number of perpendicular secondary branches in *dscam1* mutants (Figure 5J). However, the observed angle distribution was flatter than controls, but not uniform, as predicted by the "no repulsion" simulations. This suggested that self-repulsion was not completely lost in $dscam^{P1}$ mutants. Upon close inspection, indeed, instances of self-repulsion were observed in the $dscam^{P1}$ movies (Figure 5G; Video S8).

We thus modified our simulations such that the probability of switching to a depolymerizing state p_{off} was reduced upon contact. Using this modification, we tested a range of values for p_{off} although for control simulations $p_{off} = 1$ (Figure 5H). For $p_{off} =$ 0.1 (10% probability of retraction after contact), very dense arborization patterns were obtained. Increasing p_{off} resulted in decreased branch densities. Notably, for $p_{off} = 0.5$, the final dendrite morphologies are similar to control neurons (Figure 5I). Additionally, reducing p_{off} at 16 h AEL resulted in highly dense arborization patterns at 22 h AEL (for $p_{off} = 0.1$ and $p_{off} =$ 0.3). However, when p_{off} was reduced at 18 h AEL, the arborization patterns were similar to *in vivo* observations. Hence, we reduced p_{off} at 18 h AEL for further analyses.

Next, angle distribution was measured. We found that, for $p_{off} = 0.1$, the distribution was flatter than for $dscam^{P1}$ mutants, although for $p_{off} = 0.3$, it was consistent with $dscam^{P1}$ mutants (Figure 5J). We then measured the number of loops at 22 h AEL. For $p_{off} = 0.3$, the number of loops is consistent with $dscam^{P1}$ (Figure 5K), although for $p_{off} = 0.5$, there were significantly fewer loops than $dscam^{P1}$. Thus, our simulations support the experimental observation that self-repulsion is reduced, but not fully suppressed, in $dscam^{P1}$ mutants.

To conclude, self-repulsion patterns secondary branches by restricting direction of secondary extension growth, thus ensuring a preferential stabilization of secondary branches perpendicular to the primary branch, giving the class I neurons their characteristic shape.

DISCUSSION

Several studies have identified and characterized molecules important for regulating different aspects of dendrite patterning.[2,59–63] However, how a neuron integrates molecular information to generate characteristic dendrite shapes is still unclear. Addressing this type of question requires observing dendrite morphogenesis live and *in vivo*.

Previous descriptions of the embryonic development of the *Drosophila* sensory neurons showed when and how branching was initiated and completed.[62,64] However, to deepen our understanding, precise quantitative descriptions are required. The quantitative description of morphogenesis of the class I vpda neuron in our study showed that the primary dendrite grows deterministically although secondary dendrite morphogenesis is stochastic.

Our study shows that the primary dendrite could be guided by an extrinsically patterned cue present at cell-cell interfaces. Cues classically involved in axon guidance, like semaphorins,[65,66] slits,[22,24] and netrins,[25] have been implicated in dendrite targeting. Sax-7 is extrinsically patterned in *C. elegans* hypodermal cells and guides dendrite patterning of the PVD neuron. It is therefore very likely that such a molecule guides the primary dendrite of the vpda neuron.[28] Interestingly, the cell boundaries along which the primary dendrite grows appear to be stretched as junctions are aligned along the dorsal-ventral axis. Myosin II is enriched along these boundaries.[67] Thus, alternatively, cortical tension might guide the primary dorsal branch. Tension could, for instance, form a path of least resistance through local tissue deformation or provide a stiffer substratum to favor dendrite growth.[68]

Secondary dendrite morphogenesis was studied both *in vivo* and *in silico* using a computational model relying on stochastic branching dynamics, with self-repulsion. The onset of secondary branch morphogenesis was very dynamic, and as it progressed, the dynamics greatly reduced. The computational model demonstrated the necessity to incorporate a decay of kinetic parameters ("cell aging") to account for bounded dendrite growth. It is possible that dendrites age through stabilization by microtubules.[59,69] Tagged actin was expressed in the highly dynamic

(J) Probability distribution of angles between primary and secondary branches. Experiment (Expt): control n = 187; mutant n = 124 angles; Kolmogorov-Smirnov test, p = 0.011 . Simulations (Sim):p_{off} = 1.0, 0.3 and 0.1. N_{sim} = 100 .

(K) Number of loops at 22 h AEL. Expt: control n = 9; mutant n = 11 neurons. Sim:p_{off} = 1.0, 0.5 and 0.3. N_{sim} = 50. For each box, central line is median, o is the mean, the box extends vertically between the 25th and 75th percentiles, the whiskers extend to the most extreme data not considered outliers, and outliers are plotted individually.

Statistical significance calculated using Mann-Whitney U test for (C)–(E). *p < 0.05; **p < 0.01; ***p < 0.001. All the panels have the same orientation: dorsal: top; anterior: left. Scale bars represent 10 μm. See also Figure S4 and Videos S7 and S8.

dendritic tips although microtubules were present in the more stable parts of the dendritic tree (data not shown). Thus, aging could require a mechanism that decreases actin dynamics and increases microtubule polymerization over time.

Our model reveals two opposing feedbacks of tree geometry on local branch dynamics. "Child branches" (tertiary) promote branch survival by having a stabilizing effect on parent branches (secondary). Thus, branches with more children have a higher survival probability. However, a high branching density exerts a negative feedback. Self-repulsion reduces branch survival by introducing a new effective depolymerization rate k'_{off}, which is proportional to the product of encounter probability and the probability of switching to a depolymerizing state upon encounter, p_{off}. Remarkably, although all the previously described computational parameters are constitutive quantities of the model, k'_{off} is a variable parameter that depends, among others, on the local branch density. Through this "geometric" feedback, the tree architecture updates its dynamic parameters and affects its own morphogenesis. Thus, self-stabilization and self-repulsion constrain the number and lengths of the secondary branches.

vpda neuron morphogenesis has also been modeled using optimal wiring constraints and stochastic retraction[70] without explicitly incorporating self-repulsion, yet leading to similar results. This suggests that our simple rules for local dynamics could lead to optimally wired dendrite structures.

Our study revealed another remarkable function of self-repulsion in biasing the orientation of secondary dendrites perpendicular to the primary branch. The prediction from simulations was confirmed *in vivo* through the analysis of the *dscam*^{P1} mutants. During morphogenesis, growing dendrites extend and contact their neighbors. In *dscam*^{P1} mutants, dendrite growth persists in all directions, even after self-contact (Figure 5J). Thus, in controls, a given dendrite's final orientation is dependent on where and when it encountered neighbors. Hence, both experimental observations and simulations argue that the dendritic tree patterns are not guided deterministically but emerge as self-organized structures through the stochastic interactions during morphogenesis.

The *dscam*^{P1} allele is an intronic P-element insertion, which results in a strong loss-of-function allele but is not necessarily a null condition. Thus, the remnant self-repulsion we observed in *dscam*^{P1} could be the result of an incomplete loss of Dscam1. Alternatively, the remaining self-repulsion could also reflect the activity of other molecules, like multi-pass trans-membrane proteins Flamingo[71] and Wntless[72] and immunoglobulin superfamily proteins like Turtle,[73] which have all been shown to play a role in self-repulsion, albeit in other classes of md neurons. However, we cannot quantify the extent of this remnant self-repulsion and separate it from spontaneous retractions.

The *dscam*^{P1} dendrites were not longer than controls as predicted by the "no repulsion" simulations (Figure 5E). However, *dscam*^{P1} significantly increases the length of the non-orthogonally aligned dendrites (Figure S4C). Also, unlike the model prediction, the number of secondary branches in the *dscam*^{P1} mutants was significantly lower than in control dendrites (Figure S4D), suggesting a role in branch stabilization. Thus, self-repulsion may not account for all the function of Dscam1. Dscam1 is a complex molecule that could have several unknown functions. One possibility is that its loss might impinge on a signaling pathway necessary for stabilization of secondary extensions.

Although our data reveal new insights on the self-organizing properties of dendrites, our observations do not rule out the possibility that extrinsically patterned cues are also involved in secondary branch morphogenesis of vpda neurons. For example, anterior-posterior asymmetry in secondary branch length of the vpda neuron (data not shown) depends on extrinsically patterned Ten-m.[3] We suggest that self-organizing principles reported in this study could provide a "ground state" upon which additional cues could operate in other neuronal classes. The role of extrinsic cues would have to be analyzed in the background of stochastic branching processes and geometric feedbacks, which by themselves provide a spatial bias to dendrite growth. However, extrinsic cues can also profoundly control patterning as described in *C. elegans* PVD neurons.[28,38–40] Thus, the type of cue (extrinsic or intrinsic) that plays major instructive roles is context dependent.

This study highlights the dynamics of dendrite growth and provides the analytical basis for further investigating dendrite dynamics and patterning *in vivo*. It will be particularly interesting to explore, based on this study, how class-specific morphology of multi-dendritic neurons emerge as a function of varying class-specific, self-organizing rules of arborization. We suggest that such intrinsic rules, though statistical, might be genetically encoded. Ultimately, understanding how genes determine statistical rules of branching provides an opportunity to understand how, in a broader context, genes encode form.

STAR★METHODS

Detailed methods are provided in the online version of this paper and include the following:

- KEY RESOURCES TABLE
- RESOURCE AVAILABILITY
  - Lead Contact
  - Materials Availability
  - Data and Code Availability
- EXPERIMENTAL MODEL AND SUBJECT DETAILS
- METHOD DETAILS
  - Transgenic lines
  - Embryo imaging assay
  - Embryo preparation for live imaging
  - Larval preparation for live imaging
  - Immunofluorescence
  - Image acquisition
  - Laser ablations
  - Image processing and segmentation
  - Computational model
- QUANTIFICATION AND STATISTICAL ANALYSIS

SUPPLEMENTAL INFORMATION

Supplemental Information can be found online at https://doi.org/10.1016/j.cub.2020.10.054.

ACKNOWLEDGMENTS

We thank members of A.P.'s thesis jury, Markus Affolter, Edouard Hannezo, and Peter Soba for insightful comments. We thank Jean-Marc Philippe for generating the transgenic fly line and Benoit Aigouy for the "dendrite arborization tracer." We thank the IBDM imaging facility for maintenance of the

microscopes, FlyBase for maintaining curated database, and Bloomington fly facility for providing transgenic flies. A.P. was supported by Ph.D. fellowship from the LabEx INFORM (ANR-11- LABX-0054) and of the A*MIDEX project (ANR-11-IDEX-0001-02), funded by the "Investissements d'Avenir French Government program." N.T.-E. was supported by the "Investissements d'Avenir French Government program" managed by the French National Research Agency (ANR-16-CONV-0001) and from the Excellence Initiative of Aix-Marseille Univerité - A*MIDEX. We acknowledge France-BioImaging infrastructure supported by the French National Research Agency (ANR-10-INBS-04-01; «Investments for the future»).

AUTHOR CONTRIBUTIONS

Conceptualization, A.P. and T.L.; Methodology, A.P. and T.L.; Investigation, A.P. (experimental) and N.T.-E. and J.-F.R. (computational); Writing – Original Draft, A.P. and N.T.-E.; Writing – Review & Editing, A.P., T.L., N.T.-E., and J.-F.R.; Funding Acquisition, T.L.

DECLARATION OF INTERESTS

The authors declare no competing interests.

Received: July 30, 2020
Revised: September 22, 2020
Accepted: October 19, 2020
Published: November 18, 2020

REFERENCES

1. Kulkarni, V.A., and Firestein, B.L. (2012). The dendritic tree and brain disorders. Mol. Cell. Neurosci. *50*, 10–20.
2. Scott, E.K., and Luo, L. (2001). How do dendrites take their shape? Nat. Neurosci. *4*, 359–365.
3. Hattori, Y., Usui, T., Satoh, D., Moriyama, S., Shimono, K., Itoh, T., Shirahige, K., and Uemura, T. (2013). Sensory-neuron subtype-specific transcriptional programs controlling dendrite morphogenesis: genome-wide analysis of Abrupt and Knot/Collier. Dev. Cell *27*, 530–544.
4. Smith, C.J., O'Brien, T., Chatzigeorgiou, M., Spencer, W.C., Feingold-Link, E., Husson, S.J., Hori, S., Mitani, S., Gottschalk, A., Schafer, W.R., and Miller, D.M., 3rd. (2013). Sensory neuron fates are distinguished by a transcriptional switch that regulates dendrite branch stabilization. Neuron *79*, 266–280.
5. Grueber, W.B., Jan, L.Y., and Jan, Y.N. (2003). Different levels of the homeodomain protein cut regulate distinct dendrite branching patterns of Drosophila multidendritic neurons. Cell *112*, 805–818.
6. Hattori, Y., Sugimura, K., and Uemura, T. (2007). Selective expression of Knot/Collier, a transcriptional regulator of the EBF/Olf-1 family, endows the Drosophila sensory system with neuronal class-specific elaborated dendritic patterns. Genes Cells *12*, 1011–1022.
7. Sugimura, K., Satoh, D., Estes, P., Crews, S., and Uemura, T. (2004). Development of morphological diversity of dendrites in Drosophila by the BTB-zinc finger protein abrupt. Neuron *43*, 809–822.
8. Li, W., Wang, F., Menut, L., and Gao, F.B. (2004). BTB/POZ-zinc finger protein abrupt suppresses dendritic branching in a neuronal subtype-specific and dosage-dependent manner. Neuron *43*, 823–834.
9. Scott, E.K., Reuter, J.E., and Luo, L. (2003). Small GTPase Cdc42 is required for multiple aspects of dendritic morphogenesis. J. Neurosci. *23*, 3118–3123.
10. Lee, A., Li, W., Xu, K., Bogert, B.A., Su, K., and Gao, F.B. (2003). Control of dendritic development by the Drosophila fragile X-related gene involves the small GTPase Rac1. Development *130*, 5543–5552.
11. Lee, T., Winter, C., Marticke, S.S., Lee, A., and Luo, L. (2000). Essential roles of Drosophila RhoA in the regulation of neuroblast proliferation and dendritic but not axonal morphogenesis. Neuron *25*, 307–316.
12. Nakayama, A.Y., Harms, M.B., and Luo, L. (2000). Small GTPases Rac and Rho in the maintenance of dendritic spines and branches in hippocampal pyramidal neurons. J. Neurosci. *20*, 5329–5338.
13. Iyer, S.C., Wang, D., Iyer, E.P.R., Trunnell, S.A., Meduri, R., Shinwari, R., Sulkowski, M.J., and Cox, D.N. (2012). The RhoGEF trio functions in sculpting class specific dendrite morphogenesis in Drosophila sensory neurons. PLoS ONE *7*, e33634.
14. Rosário, M., Schuster, S., Jüttner, R., Parthasarathy, S., Tarabykin, V., and Birchmeier, W. (2012). Neocortical dendritic complexity is controlled during development by NOMA-GAP-dependent inhibition of Cdc42 and activation of cofilin. Genes Dev. *26*, 1743–1757.
15. Stürner, T., Tatarnikova, A., Mueller, J., Schaffran, B., Cuntz, H., Zhang, Y., Nemethova, M., Bogdan, S., Small, V., and Tavosanis, G. (2019). Transient localization of the Arp2/3 complex initiates neuronal dendrite branching *in vivo*. Development *146*, dev171397.
16. Park, M., Salgado, J.M., Ostroff, L., Helton, T.D., Robinson, C.G., Harris, K.M., and Ehlers, M.D. (2006). Plasticity-induced growth of dendritic spines by exocytic trafficking from recycling endosomes. Neuron *52*, 817–830.
17. Zou, W., Yadav, S., DeVault, L., Nung Jan, Y., and Sherwood, D.R. (2015). RAB-10-dependent membrane transport is required for dendrite arborization. PLoS Genet. *11*, e1005484.
18. Satoh, D., Sato, D., Tsuyama, T., Saito, M., Ohkura, H., Rolls, M.M., Ishikawa, F., and Uemura, T. (2008). Spatial control of branching within dendritic arbors by dynein-dependent transport of Rab5-endosomes. Nat. Cell Biol. *10*, 1164–1171.
19. Ye, B., Zhang, Y., Song, W., Younger, S.H., Jan, L.Y., and Jan, Y.N. (2007). Growing dendrites and axons differ in their reliance on the secretory pathway. Cell *130*, 717–729.
20. Cui-Wang, T., Hanus, C., Cui, T., Helton, T., Bourne, J., Watson, D., Harris, K.M., and Ehlers, M.D. (2012). Local zones of endoplasmic reticulum complexity confine cargo in neuronal dendrites. Cell *148*, 309–321.
21. Morita, A., Yamashita, N., Sasaki, Y., Uchida, Y., Nakajima, O., Nakamura, F., Yagi, T., Taniguchi, M., Usui, H., Katoh-Semba, R., et al. (2006). Regulation of dendritic branching and spine maturation by semaphorin3A-Fyn signaling. J. Neurosci. *26*, 2971–2980.
22. Furrer, M.-P., Vasenkova, I., Kamiyama, D., Rosado, Y., and Chiba, A. (2007). Slit and Robo control the development of dendrites in Drosophila CNS. Development *134*, 3795–3804.
23. Whitford, K.L., Dijkhuizen, P., Polleux, F., and Ghosh, A. (2002). Molecular control of cortical dendrite development. Annu. Rev. Neurosci. *25*, 127–149.
24. Dimitrova, S., Reissaus, A., and Tavosanis, G. (2008). Slit and Robo regulate dendrite branching and elongation of space-filling neurons in Drosophila. Dev. Biol. *324*, 18–30.
25. Matthews, B.J., and Grueber, W.B. (2011). Dscam1-mediated self-avoidance counters netrin-dependent targeting of dendrites in Drosophila. Curr. Biol. *21*, 1480–1487.
26. Furrer, M.-P., Kim, S., Wolf, B., and Chiba, A. (2003). Robo and Frazzled/DCC mediate dendritic guidance at the CNS midline. Nat. Neurosci. *6*, 223–230.
27. Teichmann, H.M., and Shen, K. (2011). UNC-6 and UNC-40 promote dendritic growth through PAR-4 in Caenorhabditis elegans neurons. Nat. Neurosci. *14*, 165–172.
28. Dong, X., Liu, O.W., Howell, A.S., and Shen, K. (2013). An extracellular adhesion molecule complex patterns dendritic branching and morphogenesis. Cell *155*, 296–307.
29. Lanoue, V., Usardi, A., Sigoillot, S.M., Talleur, M., Iyer, K., Mariani, J., Isope, P., Vodjdani, G., Heintz, N., and Selimi, F. (2013). The adhesion-GPCR BAI3, a gene linked to psychiatric disorders, regulates dendrite morphogenesis in neurons. Mol. Psychiatry *18*, 943–950.
30. Han, C., Wang, D., Soba, P., Zhu, S., Lin, X., Jan, L.Y., and Jan, Y.N. (2012). Integrins regulate repulsion-mediated dendritic patterning of Drosophila sensory neurons by restricting dendrites in a 2D space. Neuron *73*, 64–78.

31. Gaudillière, B., Konishi, Y., de la Iglesia, N., Yao, G.l., and Bonni, A. (2004). A CaMKII-NeuroD signaling pathway specifies dendritic morphogenesis. Neuron *41*, 229–241.

32. Puram, S.V., Kim, A.H., Ikeuchi, Y., Wilson-Grady, J.T., Merdes, A., Gygi, S.P., and Bonni, A. (2011). A CaMKIIβ signaling pathway at the centrosome regulates dendrite patterning in the brain. Nat. Neurosci. *14*, 973–983.

33. Wang, S., Sekiguchi, R., Daley, W.P., and Yamada, K.M. (2017). Patterned cell and matrix dynamics in branching morphogenesis. J. Cell Biol. *216*, 559–570.

34. Hannezo, E., Scheele, C.L.G.J., Moad, M., Drogo, N., Heer, R., Sampogna, R.V., van Rheenen, J., and Simons, B.D. (2017). A unifying theory of branching morphogenesis. Cell *171*, 242–255.e27.

35. Metzger, R.J., and Krasnow, M.A. (1999). Genetic control of branching morphogenesis. Science *284*, 1635–1639.

36. Metzger, R.J., Klein, O.D., Martin, G.R., and Krasnow, M.A. (2008). The branching programme of mouse lung development. Nature *453*, 745–750.

37. Samakovlis, C., Hacohen, N., Manning, G., Sutherland, D.C., Guillemin, K., and Krasnow, M.A. (1996). Development of the Drosophila tracheal system occurs by a series of morphologically distinct but genetically coupled branching events. Development *122*, 1395–1407.

38. Salzberg, Y., Díaz-Balzac, C.A., Ramirez-Suarez, N.J., Attreed, M., Tecle, E., Desbois, M., Kaprielian, Z., and Bülow, H.E. (2013). Skin-derived cues control arborization of sensory dendrites in Caenorhabditis elegans. Cell *155*, 308–320.

39. Zou, W., Shen, A., Dong, X., Tugizova, M., Xiang, Y.K., and Shen, K. (2016). A multi-protein receptor-ligand complex underlies combinatorial dendrite guidance choices in *C. elegans*. eLife *5*, 1–25.

40. Díaz-Balzac, C.A., Rahman, M., Lázaro-Peña, M.I., Martin Hernandez, L.A., Salzberg, Y., Aguirre-Chen, C., Kaprielian, Z., and Bülow, H.E. (2016). Muscle- and skin-derived cues jointly orchestrate patterning of somatosensory dendrites. Curr. Biol. *26*, 2379–2387.

41. Ochoa-Espinosa, A., and Affolter, M. (2012). Branching morphogenesis: from cells to organs and back. Cold Spring Harb. Perspect. Biol. *4*, 1–14.

42. Gjorevski, N., and Nelson, C.M. (2011). Integrated morphodynamic signalling of the mammary gland. Nat. Rev. Mol. Cell Biol. *12*, 581–593.

43. Campos-Ortega, J.A. (1997). Asymmetic division: dynastic intricacies of neuroblast division. Curr. Biol. *7*, R726–R728.

44. Freeman, M. (1996). Reiterative use of the EGF receptor triggers differentiation of all cell types in the Drosophila eye. Cell *87*, 651–660.

45. Changeux, J.-P., and Danchin, A. (1976). Selective stabilisation of developing synapses as a mechanism for the specification of neuronal networks. Nature *264*, 705–712.

46. Macagno, E.R., Lopresti, V., and Levinthal, C. (1973). Structure and development of neuronal connections in isogenic organisms: variations and similarities in the optic system of Daphnia magna. Proc. Natl. Acad. Sci. USA *70*, 57–61.

47. Goodman, C.S., Pearson, K.G., and Heitler, W.J. (1979). Variability of identified neurons in grasshoppers. Comp. Biochem. Physiol. Part A. Physiol. *64*, 455–462.

48. Bodmer, R., and Jan, Y.N. (1987). Morphological differentiation of the embryonic peripheral neurons in Drosophila. Rouxs Arch. Dev. Biol. *196*, 69–77.

49. Grueber, W.B., Ye, B., Moore, A.W., Jan, L.Y., and Jan, Y.N. (2003). Dendrites of distinct classes of Drosophila sensory neurons show different capacities for homotypic repulsion. Curr. Biol. *13*, 618–626.

50. Grueber, W.B., Jan, L.Y., and Jan, Y.N. (2002). Tiling of the Drosophila epidermis by multidendritic sensory neurons. Development *129*, 2867–2878.

51. Gao, F.B., Kohwi, M., Brenman, J.E., Jan, L.Y., and Jan, Y.N. (2000). Control of dendritic field formation in Drosophila: the roles of flamingo and competition between homologous neurons. Neuron *28*, 91–101.

52. Iyer, E.P.R., Iyer, S.C., Sullivan, L., Wang, D., Meduri, R., Graybeal, L.L., and Cox, D.N. (2013). Functional genomic analyses of two morphologically distinct classes of Drosophila sensory neurons: post-mitotic roles of transcription factors in dendritic patterning. PLoS ONE *8*, e72434.

53. Parrish, J.Z., Xu, P., Kim, C.C., Jan, L.Y., and Jan, Y.N. (2009). The microRNA bantam functions in epithelial cells to regulate scaling growth of dendrite arbors in Drosophila sensory neurons. Neuron *63*, 788–802.

54. Shimono, K., Fujishima, K., Nomura, T., Ohashi, M., Usui, T., Kengaku, M., Toyoda, A., and Uemura, T. (2014). An evolutionarily conserved protein CHORD regulates scaling of dendritic arbors with body size. Sci. Rep. *4*, 4415.

55. Schmucker, D., Clemens, J.C., Shu, H., Worby, C.A., Xiao, J., Muda, M., Dixon, J.E., and Zipursky, S.L. (2000). Drosophila Dscam is an axon guidance receptor exhibiting extraordinary molecular diversity. Cell *101*, 671–684.

56. Soba, P., Zhu, S., Emoto, K., Younger, S., Yang, S.J., Yu, H.H., Lee, T., Jan, L.Y., and Jan, Y.N. (2007). Drosophila sensory neurons require Dscam for dendritic self-avoidance and proper dendritic field organization. Neuron *54*, 403–416.

57. Matthews, B.J., Kim, M.E., Flanagan, J.J., Hattori, D., Clemens, J.C., Zipursky, S.L., and Grueber, W.B. (2007). Dendrite self-avoidance is controlled by Dscam. Cell *129*, 593–604.

58. Hughes, M.E., Bortnick, R., Tsubouchi, A., Bäumer, P., Kondo, M., Uemura, T., and Schmucker, D. (2007). Homophilic Dscam interactions control complex dendrite morphogenesis. Neuron *54*, 417–427.

59. Menon, S., and Gupton, S. (2018). Recent advances in branching mechanisms underlying neuronal morphogenesis. F1000Res. *7*, 1–12.

60. Singhania, A., and Grueber, W.B. (2014). Development of the embryonic and larval peripheral nervous system of Drosophila. Wiley Interdiscip. Rev. Dev. Biol. *3*, 193–210.

61. Jan, Y.-N., and Jan, L.Y. (2010). Branching out: mechanisms of dendritic arborization. Nat. Rev. Neurosci. *11*, 316–328.

62. Gao, F.B., Brenman, J.E., Jan, L.Y., and Jan, Y.N. (1999). Genes regulating dendritic outgrowth, branching, and routing in Drosophila. Genes Dev. *13*, 2549–2561.

63. Dong, X., Shen, K., and Bülow, H.E. (2015). Intrinsic and extrinsic mechanisms of dendritic morphogenesis. Annu. Rev. Physiol. *77*, 271–300.

64. Sugimura, K., Yamamoto, M., Niwa, R., Satoh, D., Goto, S., Taniguchi, M., Hayashi, S., and Uemura, T. (2003). Distinct developmental modes and lesion-induced reactions of dendrites of two classes of Drosophila sensory neurons. J. Neurosci. *23*, 3752–3760.

65. Komiyama, T., Sweeney, L.B., Schuldiner, O., Garcia, K.C., and Luo, L. (2007). Graded expression of semaphorin-1a cell-autonomously directs dendritic targeting of olfactory projection neurons. Cell *128*, 399–410.

66. Shen, H.-C., Chu, S.-Y., Hsu, T.-C., Wang, C.-H., Lin, I.-Y., and Yu, H.-H. (2017). Semaphorin-1a prevents Drosophila olfactory projection neuron dendrites from mis-targeting into select antennal lobe regions. PLoS Genet. *13*, e1006751.

67. Lawlor, K.T., Ly, D.C., and DiNardo, S. (2013). Drosophila Dachsous and Fat polarize actin-based protrusions over a restricted domain of the embryonic denticle field. Dev. Biol. *383*, 285–294.

68. Franze, K. (2020). Integrating chemistry and mechanics: the forces driving axon growth. Annu. Rev. Cell Dev. Biol. *36*, 61–83.

69. Puram, S.V., and Bonni, A. (2013). Cell-intrinsic drivers of dendrite morphogenesis. Development *140*, 4657–4671.

70. Castro, A.F., Baltruschat, L., Stürner, T., Bahrami, A., Jedlicka, P., Tavosanis, G., and Cuntz, H. (2020). Achieving functional neuronal dendrite structure through sequential stochastic growth and retraction. bioRxiv. https://doi.org/10.1101/2020.07.09.195446.

71. Matsubara, D., Horiuchi, S.Y., Shimono, K., Usui, T., and Uemura, T. (2011). The seven-pass transmembrane cadherin Flamingo controls dendritic self-avoidance via its binding to a LIM domain protein, Espinas, in Drosophila sensory neurons. Genes Dev. *25*, 1982–1996.

72. Liao, C.P., Li, H., Lee, H.H., Chien, C.T., and Pan, C.L. (2018). Cell-autonomous regulation of dendrite self-avoidance by the Wnt secretory factor MIG-14/Wntless. Neuron *98*, 320–334.e6.

73. Long, H., Ou, Y., Rao, Y., and van Meyel, D.J. (2009). Dendrite branching and self-avoidance are controlled by Turtle, a conserved IgSF protein in Drosophila. Development *136*, 3475–3484.

74. Parrish, J.Z., Kim, M.D., Jan, L.Y., and Jan, Y.N. (2006). Genome-wide analyses identify transcription factors required for proper morphogenesis of Drosophila sensory neuron dendrites. Genes Dev. *20*, 820–835.

75. O'Donnell, P.T., and Bernstein, S.I. (1988). Molecular and ultrastructural defects in a Drosophila myosin heavy chain mutant: differential effects on muscle function produced by similar thick filament abnormalities. J. Cell Biol. *107*, 2601–2612.

76. Yu, D., Baird, M.A., Allen, J.R., Howe, E.S., Klassen, M.P., Reade, A., Makhijani, K., Song, Y., Liu, S., Murthy, Z., et al. (2015). A naturally monomeric infrared fluorescent protein for protein labeling in vivo. Nat. Methods *12*, 763–765.

77. Schindelin, J., Arganda-Carreras, I., Frise, E., Kaynig, V., Longair, M., Pietzsch, T., Preibisch, S., Rueden, C., Saalfeld, S., Schmid, B., et al. (2012). Fiji: an open-source platform for biological-image analysis. Nat. Methods *9*, 676–682.

78. Li, W., and Gao, F.-B. (2003). Actin filament-stabilizing protein tropomyosin regulates the size of dendritic fields. J. Neurosci. *23*, 6171–6175.

79. Pilot, F., Philippe, J.M., Lemmers, C., Chauvin, J.P., and Lecuit, T. (2006). Developmental control of nuclear morphogenesis and anchoring by charleston, identified in a functional genomic screen of Drosophila cellularisation. Development *133*, 711–723.

80. Parton, R.M., Valles, A.M., Dobbie, I.M., and Davis, I. (2010). Drosophila larval fillet preparation and imaging of neurons. Cold Spring Harb. Protoc. *2010*, pdb.prot5405.

81. Gittes, F., Mickey, B., Nettleton, J., and Howard, J. (1993). Flexural rigidity of microtubules and actin filaments measured from thermal fluctuations in shape. J. Cell Biol. *120*, 923–934.

Please cite this article in press as: Palavalli et al., Deterministic and Stochastic Rules of Branching Govern Dendrite Morphogenesis of Sensory Neurons, Current Biology (2020), https://doi.org/10.1016/j.cub.2020.10.054

STAR★METHODS

KEY RESOURCES TABLE

REAGENT or RESOURCE	SOURCE	IDENTIFIER
Antibodies		
Rabbit polyclonal anti-GFP	Thermo Fisher Scientific	Cat # PA1-980A; RRID:AB_325960
Goat anti-Rabbit Alexa Fluor® 488	Thermo Fisher Scientific	Cat # A32731; RRID:AB_2633280
Chemicals, Peptides, and Recombinant Proteins		
Ryanodine	Merck	Cat# 559276-500UG
Experimental Models: Organisms/Strains		
D. melanogaster . 2-21 gal4	[74]	Flybase ID: FBal0328157
*D. melanogaster. mhc*1	[75]	Flybase ID: FBal0012242
D.melanogaster. UAS-CD8::GFP y [1] w[*]; P{w[+mC] = UAS-mCD8::GFP.L}LL5, P{UAS-mCD8::GFP.L}2	Bloomington Drosophila Stock Center	BDSC:5137 Flybase ID: FBti0012685
D. melanogaster: Ecad::Tomato y[1] w[*]; TI{TI}shg[mTomato]	Bloomington Drosophila Stock Center	BDSC: 58789 Flybase ID: FBti0168570
D. melanogaster. $dscam^{P1}$ P{ry [+t7.2] = PZ}Dscam1[05518] cn^{1}/ CyO; ry[506]	Bloomington Drosophila Stock Center	BDSC: 11412 Flybase ID: FBti0002607
D. melanogaster: ΔDscam1 w [1118]; Df(2R)ED1673, P{w [+mW.Scer\FRT.hs3] = 3′.RS5+3.3′} ED1673/SM6a	Bloomington Drosophila Stock Center	BDSC: 9062 Flybase ID: FBab0032981
D. melanogaster. UAS-CD4::neongreen	This paper	N/A
Recombinant DNA		
pACU2_CD4-mIFP T2A HO1	[76]	RRID:Addgene_72441
Software and Algorithms		
MATLAB R2018a	MathWorks	RRID:SCR_001622
Fiji	[77]	RRID:SCR_002285 https://fiji.sc
Dendrite Arborization Tracer	This paper	https://github.com/baigouy/DAT/

RESOURCE AVAILABILITY

Lead Contact

Further information and requests for resources and reagents should be directed to and will be fulfilled by the Lead Contact, Thomas Lecuit (thomas.lecuit@univ-amu.fr).

Materials Availability

This study did not generate new unique reagents.

Data and Code Availability

The codes for the Dendrite Arborization Tracer tool generated during this study are available at github: https://github.com/baigouy/DAT/. The codes generated for computational modeling will be available upon request to jean-francois.rupprecht@cpt.univ-mrs.fr

EXPERIMENTAL MODEL AND SUBJECT DETAILS

The experiments were performed on *Drosophila melanogaster* embryos and larvae. The adult flies were maintained under the standard lab conditions in plastic vials at 18°C or 25°C with yeast food. Embryo collection was done in fly cages with agar plates made with apple juice, supplemented with yeast paste. Flies lay eggs on these plates and embryos are filtered from the yeast paste with distilled water. Larvae were grown in plastic vials at 25°C and collected at 24h, 48h, 72h and 96h AEL.

Please cite this article in press as: Palavalli et al., Deterministic and Stochastic Rules of Branching Govern Dendrite Morphogenesis of Sensory Neurons, Current Biology (2020), https://doi.org/10.1016/j.cub.2020.10.054

METHOD DETAILS

Transgenic lines

All fly lines used in this study are listed in the Key Resources Table. To generate the UAS-CD4::neongreen flies, pACU2_CD4-mIFP T2A HO1 from Xiaokun Shu[76] ordered from ADDGENE (72441) was modified. The open reading frame (ORF) part corresponding to mIFP-T2A-HO1 was replaced by mNeonGreen's ORF, producing a Cter mNeonGreen tagged version of the human transmembrane protein CD4. Expression plasmid named pACU-CD4-NeonGreen was verified by sequencing (Genewiz) and sent to Bestgene Inc. to perform transgenesis into attP-containing docking site strains attP2 (3L, 68A4). Sequence of the plasmid is available upon request.

Embryo imaging assay

The muscular tissue is established at the stage at which neuron morphogenesis occurs; hence, muscle contraction prevented the capture of stable and time resolved images. A previous study suggested dendrite development was normal in mutants for muscle myosin, which paralyzes embryos[78]. Therefore, vpda neurons labeled with CD8::GFP (using the 2-21Gal-4 driver line[74]) were imaged in a muscle myosin heavy chain mutant background[75] to prevent muscular contractions. No statistically significant difference in neuron morphology was observed in *mhc*1 mutant embryos (Figure S1E–S1H), suggesting that *mhc*1 mutants provide an effective solution to temporally resolve embryonic dendrite morphologies.

When, recombining the *mhc*1 mutant allele with the $dscam^{P1}$ mutant proved to be difficult; in these experiments, Ryanodine (a drug that inhibits muscle contractions by binding to the ryanodine receptor and preventing calcium release into the sarcoplasmic reticulum) was injected into stage 16 embryos. Single images of water and ryanodine injected vpda neurons were captured 10 hours after injection. Analysis revealed no major defects in dendrite morphology, apart from small but significant increase in the number of secondary branches in the ryanodine injected embryos (Figure S1I–S1L). As there were no other patterning differences, the ryanodine-injected embryos still offered an effective solution to obtain time resolved images of $dscam^{P1}$ mutant embryos. In Ryanodine injected embryos, muscle contractions are reduced but not completely gone, thus, the out of focus images are deleted from the movies.

Embryo preparation for live imaging

Embryos were prepared as described before[79]. In brief, embryos were de-chorionated using bleach, for about 1 minute and then washed thoroughly with distilled water. The embryos were then aligned ventro-laterally on a flat piece of agar and then glued to a glass coverslip. These embryos can be submerged in halocarbon oil and imaged directly. Alternatively, glued embryos (;$dscam^{P1}$/ΔDscam1;2-21 gal4, UAS-CD4::neongreen/''; 2-21 gal4 and ;;UAS-CD8::GFP/''; 2-21 gal4) were kept in an airtight box containing Drierite for about 7 min, then covered in halocarbon oil, and then injected with Ryanodine. Ryanodine was injected at a concentration of 50mM in mid stage 16 embryos about 10 minutes prior to imaging using a FemtoJet 4i microinjector by Eppendorf and then imaged at the microscope.

Larval preparation for live imaging

For analysis of dendrite morphology at different stages of development, whole larvae at L1, L2 and L3 were placed in a watch glass with a few mL of 1mM Sodium Azide to paralyze them and then mounted in low melting agarose to be imaged on a lightsheet microscope so that the larvae could be rotated and all the neurons could be easily imaged.

Immunofluorescence

Homozygous 2-21 gal4/UAS-mCD8::GFP larvae (96h ± 3) were filleted using standard protocols[80] Briefly, the larvae were washed with PBS and pinned on PDMS plates, keeping the dorsal side upright, with dissection pins between the mouth hooks and posterior spiracles. Fine dissecting scissors were used to open the larvae along the center from posterior to anterior. Forceps were used to carefully remove the gut. The anterior and posterior ends were then pinned laterally to obtain the fillet and fixed in 4%PFA for 15min and stained with a rabbit anti-GFP antibody (1:500,). Secondary antibodies conjugates with Alexa488, were used 1:500. The stained larvae were mounted in VECTASHIELD®.

Image acquisition

For live imaging, embryos were prepared as described earlier and time-lapse imaging was performed with a dual camera spinning disc (CSU-X1, Yokogawa) Nikon Eclipse Ti inverted microscope (distributed by Roper) using a 100X/N.A 1.4 oil-immersion objective. The system acquires images using the Meta-Morph software and images were taken as z series of 1.5 μm X10 planes spanning 13.5 μm and acquired with a frame rate of 3min for 10hours (Figure 1D) or 30min for 10 hours (Figure 2C) or 30 s for 1hour (Figure 3F).

For whole mount imaging, larvae were treated as described before and imaged on a Zeiss Lightsheet Z.1 on a 20X/N.A 0.8. The system acquires images using ZEN software conditions were kept consistent for all 3 stages.

Fixed larval fillets were imaged on a Zeiss LSM 880 on a 25X/N.A 0.8. The system acquires images using the ZEN software and image stacks with spacing of 0.15–0.2 μm were collected and stack focused projections of 7-10 planes analyzed.

Laser ablations

Ablations were performed at around 15-16h AEL on an inverted microscope (Eclipse TE 2000-E; Nikon) equipped with a spinning-disc (Ultraview ERS, Perkin Elmer) for fast imaging. Time lapse at a single z-plane was acquired using a 100X/ NA 1.4 oil immersion objective. Ablations were performed in parallel with image acquisition. Ablation events were obtained by exposing the primary

Please cite this article in press as: Palavalli et al., Deterministic and Stochastic Rules of Branching Govern Dendrite Morphogenesis of Sensory Neurons, Current Biology (2020), https://doi.org/10.1016/j.cub.2020.10.054

dendrite, for duration of 2–3 ms, to a near-infrared laser (1030 nm) focused in a diffraction-limited spot. Laser power at the back aperture of the objective was ~400mW. Once ablated, the neurons were imaged on the dual camera, spinning disc (CSU-X1, Yokogawa) Nikon Eclipse Ti inverted microscope (distributed by Roper) using a 100X/N.A 1.4 oil-immersion objective as described above. In these experiments, the control neurons were the unablated neurons from the neighboring segments.

Image processing and segmentation

CD8::GFP or CD4::neongreen was used to label the neuronal cell membranes. A custom ImageJ macro integrating the Stack Focuser plugin from M. Umorin was used to project (by maximum intensity projection the z-planes with signal from the neuron. This resulted in sharper cell outlines and better S/N ratio compared with maximal projections. The 2D projected stacks were then segmented using a custom 'Dendritic Arborization Tracer' from B. Aigouy.

The 'Dendrite Arborization Tracer' provides skeletonized images in such a way that every segment (connected to other segments through vertices) is assigned a unique identity (Figure S1B). We then ordered these individual segments using MATLAB (including Curve Fitting Toolbox, Image Processing Toolbox, Statistics and Machine Learning Toolbox). Starting from the cell body we connected segments that made the longest line and assigned it to be the primary branch. Similarly, we then connected all the segments making the longest lines starting from the primary branch to be secondary branches and so on (Figures S1A–S1C). However, our code does account for loops in the dendritic tree. In the wild-type, the dendrites rarely crossed each other, however, in the event of a crossing, we manually removed the loops (only when we looked at normal growth (Figure 1)). We then performed all our analysis on this processed skeleton of the dendrite. To plot data, we used MATLAB (the IoSR boxplot function by Christopher Hummersone).

When we compared control and *dscam1* mutants, loops in the dendritic tree prevented us from using the software, thus, the movies of development in both conditions were segmented using the 'Dendrite Arborization Tracer' but the dendrites were ordered manually by observing the movies of embryonic development.

Computational model

We developed a two-dimensional stochastic branching model with contact-induced branch depolymerization (or self-repulsion). In contrast to other branching models for morphogenesis[34], we include the possibility of branch retraction.

In our simulations, the dendrite structure is discretized into elementary spatial units (hereafter referred to as beads). At the simulation time $t = 0$ (approximately corresponding to the developmental time $t = 15$h AEL), we consider a pre-existing primary branch composed of a constant number of beads $N_1 = 100$ (corresponding to $L_1 = 30\mu$m) and situated along the y axis.

Branching

At each time step Δt, a new secondary branch is created from an un-branched bead with a probability denoted by

$$P_{b,2} = \lambda_1 \Delta l_1 \Delta t,$$

where Δl_1 is the inter-bead spacing on the primary branch; λ_1 is the branching rate of secondary branches. After 1h of evolution (corresponding to t = 16h AEL), tertiary and quaternary branches are created using the same mechanism. Similarly, we define the per-bead new tertiary (resp. quaternary) branch creation probability $P_{b,3} = \lambda_2 \Delta l_2 \Delta t$ from a secondary bead (resp. $P_{b,4} = \lambda_3 \Delta l_3 \Delta t$ from a tertiary bead), where $\Delta l_{2/3}$ is the bead interspacing for secondary (resp. tertiary) branches and $\lambda_{2/3}$ is the branching rate of tertiary (resp. quaternary) branches. Whenever a new branch (called a child branch) is created, we place the first bead of the newly created child branch at the coordinate location:

$$x_{i,child} = x_{parent} + \Delta l_i \cos\theta$$

$$y_{i,child} = y_{parent} + \Delta l_i \sin\theta$$

where (x_{parent}, y_{parent}) is the coordinate of the parent bead, the index i stands for the order of complexity of the branch and θ is chosen according to a uniform distribution on $[0, 2\pi]$.

Polymerization/depolymerization

We assume that branches are constantly either in a polymerizing or a depolymerizing state. A branch in a polymerizing state grows with a rate $v_{i,on}$, where the index i again stands for the order of complexity of the extension. In this way, at each time step Δt the number of beads of the branch is increased by one. The position of the new bead j is:

$$x_{i,j} = x_{i,j-1} + \Delta l_i \cos\varphi_{i,j}$$

$$y_{i,j} = y_{i,j-1} + \Delta l_i \sin\varphi_{i,j}$$

$$\varphi_{i,j} = \varphi_{i,j-1} + \sqrt{\frac{2\Delta l_i}{l_p}}\eta$$

Please cite this article in press as: Palavalli et al., Deterministic and Stochastic Rules of Branching Govern Dendrite Morphogenesis of Sensory Neurons, Current Biology (2020), https://doi.org/10.1016/j.cub.2020.10.054

where $(x_{i,j-1}, y_{i,j-1})$ is the position of the previous bead in the branch, η is a centered unit Gaussian variable and l_p is the persistence length of the dendrite branch. We considered a persistence length of $l_p = 17\mu m$, which is consistent with values measured in the actin bundles[81] (see Table 1).

Conversely, a branch in a depolymerizing state shrinks with a rate $v_{i,off}$. Experimental branch tracking suggest that we can set $v_{i,on} = v_{i,off}$. Depolymerization occurs through removal of beads at the branch tip. We prevent branch depolymerization beyond a forking bead. If a child was created from this bead, the parent branch changes to a polymerizing state and starts to grow again. A branch disappears if its last bead is removed through depolymerization.

Spontaneous switching

We define the rates k_{on} (resp. k_{off}) for branches to switch from a depolymerizing (resp. polymerizing) state to a polymerizing (resp. depolymerizing) one. In our simulation, at each time step Δt we evaluate whether a branch should switch from a depolymerizing state to a polymerizing state; the switch occurs stochastically every time we find that a random variable uniformly distributed on (0,1), denoted U, satisfies the relation:

$$U < 1 - e^{-k_{on}\Delta t}.$$

Therefore, the mean duration of polymerization phases read $\tau_{on} = 1/k_{on}$. Similarly, the statistics of the switch from polymerization to depolymerization is evaluated according to a rate denoted by k_{off} (and τ_{off}).

Contact-induced depolymerization

Whenever the distance between the last new bead of a polymerizing branch and any bead of other branches is smaller than a certain threshold d_{th}, depolymerization is implemented with probability p_{off}. The case $p_{off} = 1$ corresponds to the control case; we find that $p_{off} = 0.3$ provides a satisfactory fit for $dscam^{P1}$ mutants.

Aging

We implemented a progressive reduction of the values of the dynamic parameters at regular time intervals (corresponding to 2h *in vivo*). In particular, both the branching and switching rates, λ_i and $k_{i,on/off}$ respectively, are reduced by a factor f_i, with i being the order of complexity of the branch, while the polymerizing and depolymerizing rates, $v_{i,on/off}$, are reduced by a different factor $f_{v,i}$. At each reduction, we re-mesh each branch with a new interspacing given by $v_{i,on} f_{v,i} \Delta t$ (with $v_{i,on}$ the initial growth rate), which amounts to increasing the number of beads. The interplay between the possible values of f_i and $f_{v,i}$ defines the two aging protocols presented in the main text (see also Figure 4D).

QUANTIFICATION AND STATISTICAL ANALYSIS

For all experiments data points from different neurons/embryos from at least 3 independent experiments were pooled. For each box, in the boxplots, the central line is the median, the 'o' is the mean, the box extends vertically between the 25th and 75th percentiles, the whiskers extend to the most extreme data that are not considered outliers, and the outliers are plotted individually. All the P values are calculated using a two-sided non-parametric Mann–Whitney test (MATLAB statistics toolbox) except in Figure 5J where P values are calculated using the two sample Kolmogorov-Smirnov test. The exact values of n and what it represents for each graph are reported in the figure legends. The experiments were not randomized and the investigators were not blinded to allocation during experiments and outcome assessment.

Current Biology, Volume *31*

Supplemental Information

Deterministic and Stochastic Rules of Branching Govern Dendrite Morphogenesis of Sensory Neurons

Amrutha Palavalli, Nicolás Tizón-Escamilla, Jean-François Rupprecht, and Thomas Lecuit

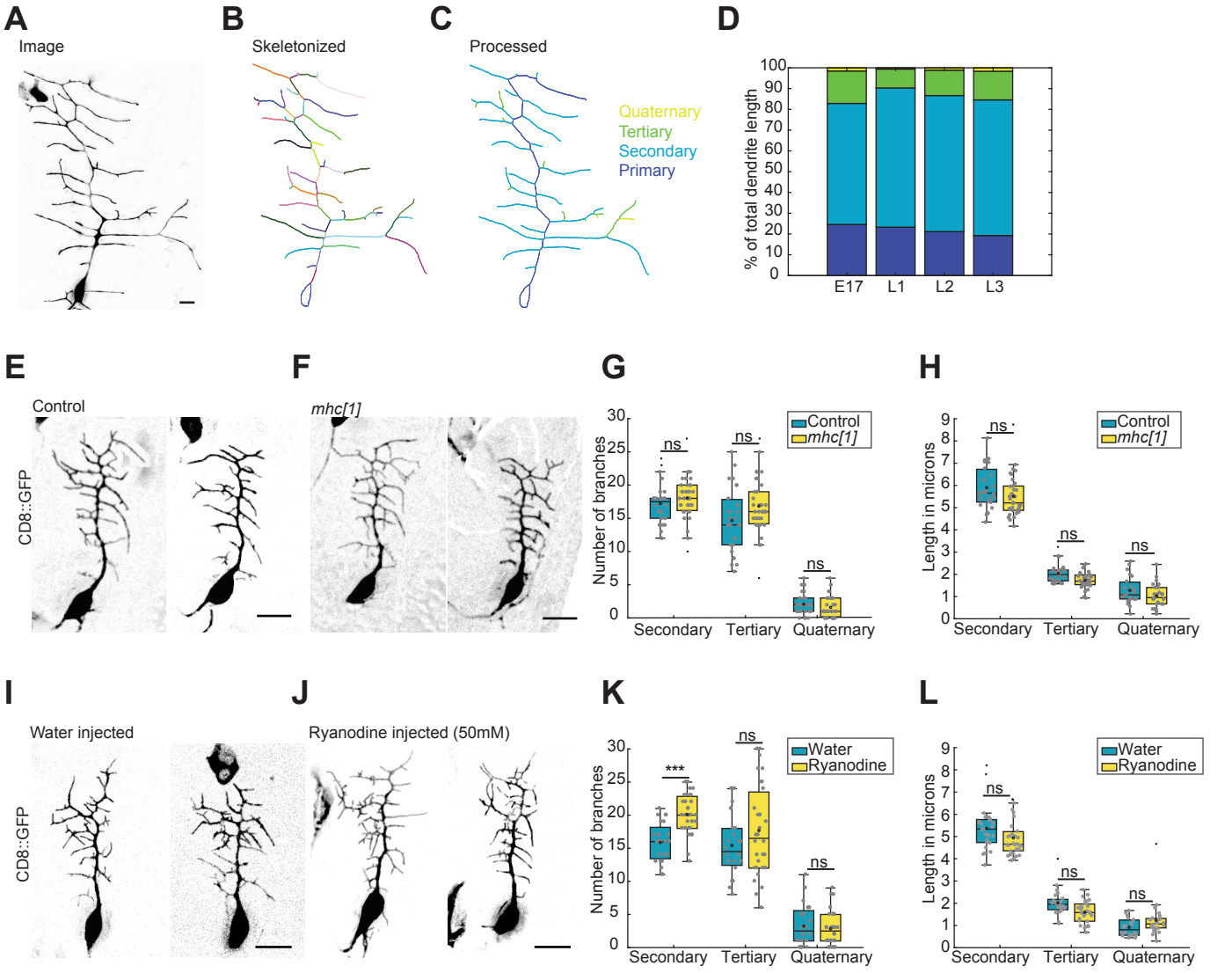

Figure S1. Branch ordering class I vpda neuron and blocking muscular contractions. Related to Figure 1 and Figure 5 and STAR Methods.

(A) Class I vpda neuron at the 3rd instar (L3 72h AEL±3) (B) Skeletonized neuron obtained from 'Dendrite Arborization Tracer'. Every segment (length of dendrite between two vertices) has a unique identity represented by different colours. (C) Processed dendrite classified into 4 orders of complexity. Primary (Indigo), Secondary (blue), Tertiary (green), Quaternary (yellow). (D) Percentage composition of total dendrite length. E17 n=26, L1 n=48, L2 n=50 L3 n=38 neurons (E) Control Class I vpda neurons from homozygous 2-21gal4/UAS-mCD8::GFP embryos (20h AEL±3). (F) Class I vpda neurons from 2-21gal4/UAS-mCD8::GFP, mhc[1] mutant embryos (20h AEL±3). (G) Number of branches at each order of complexity (H) Branch lengths at each order of complexity. For (G) and (H) Control (Blue) n=27 mhc[1] mutant (yellow) n=35 neurons. (I) Class I vpda neurons injected with water (J) Class I vpda neurons injected with Ryanodine. For (I) and (J) embryos were taken from homozygous 2-21gal4/UAS-mCD8::GFP (K) Number of branches at each order of complexity. (L) Branch lengths at each order of complexity. For (K) and (L) Water (blue) n=24 Ryanodine (yellow) n=31. For each box, the central line is the median, the 'o' is the mean, the box extends vertically between the 25th and 75th percentiles, the whiskers extend to the most extreme data that are not considered outliers, and the outliers are plotted individually. Statistical significance has been calculated using Mann-Whitney U test. ns, * $p<0.05$; ** $p<0.01$, *** $p<0.001$. All the panels have the same orientation: dorsal at the top, anterior to the left. Scale bars = 10μm.

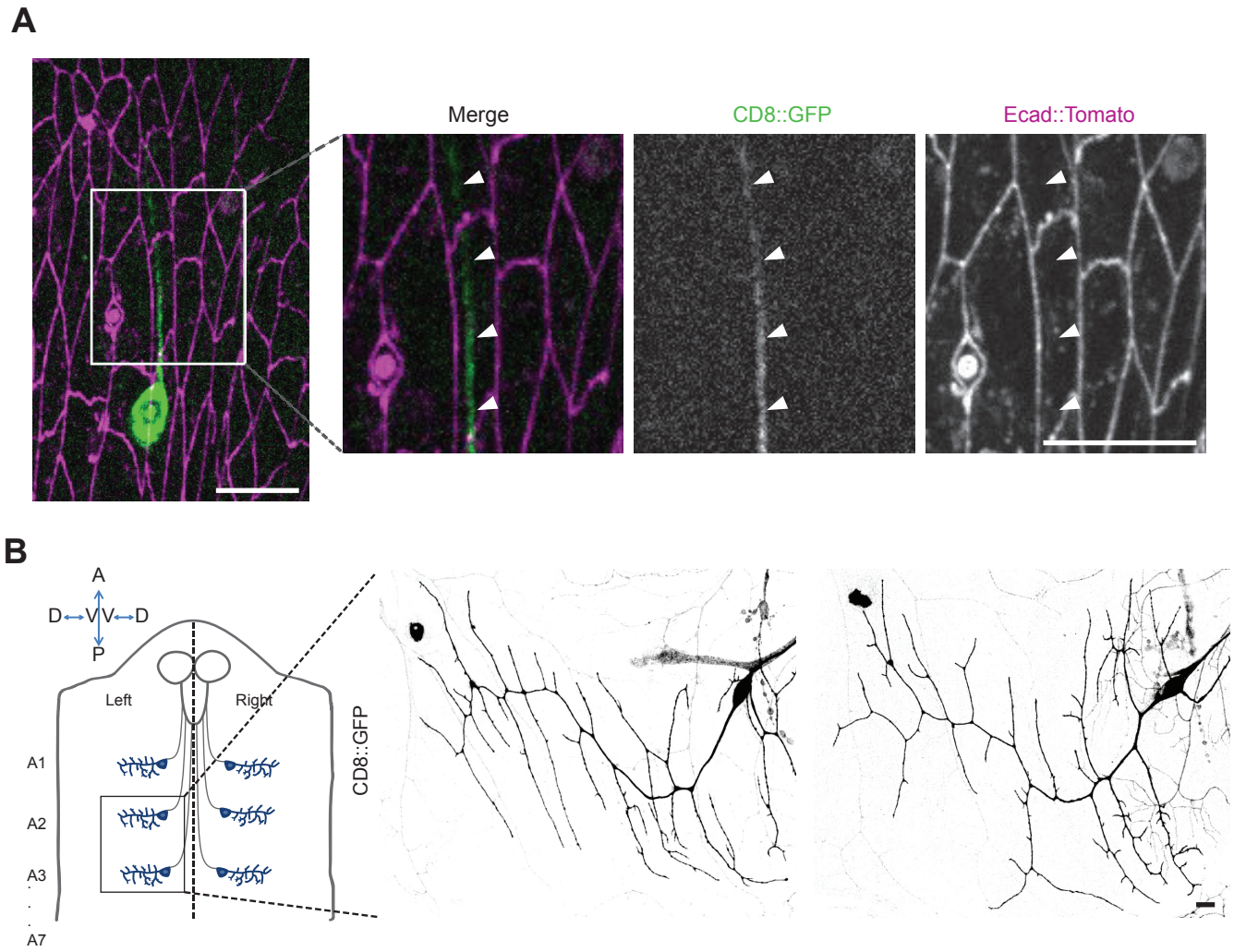
A
Merge
CD8::GFP
Ecad::Tomato
B
A
D
V
V
D
P
Left
Right
A1
A2
A3
A7
CD8::GFP
C
Distribution of secondary branch numbers
A3 and A2
mean:18.24
sd:2.75
Number of neurons
Number of branches
D
Distribution of A2-A3 difference
in secondary branch number
mean:0.8
sd:3.5
Number of pairs
Number of branches
E
CD4::neongreen
00:00
00:06
00:12
00:18
00:24
00:30
00:36
00:42
00:48
00:54
01:00
01:06
01:12
01:18
01:24 h:min

Figure S2. Primary branch remains parallel to the stretched E-cadherin cell boundaries and Difference between dendritic trees on abdominal segment A2 and A3. Related to Figure 2, 3 and 4 and Video S6.

(A) Image of neuron at ~15h AEL co-imaged with Ecad::tomato. Inset: Close up of primary dendrite parallel to stretched E-cadherin cell boundaries as indicated by the white arrowheads. Taken from live homozygous 2-21gal4/UAS-mCD8::GFP, Ecad::tomato embryos (B) Schematic of a Larval filet (indicating vpda neurons in the abdominal hemi segments. Neurons in segment A2 and A3 on the left hemi-segment were used for analysis. A2 (left panel) A3 (right panel) vpda neurons at 96h AEL ±3 from homozygous 2-21gal4/UAS-mCD8::GFP larvae. The panel has the following orientation: Anterior at the top, Posterior at the bottom, ventral is the center and dorsal to the sides (C) Distribution of the total number of Secondary Branches n=42 neurons (21 A2-A3 pairs). (D) Distribution of difference in number of Secondary branches between the A2-A3 pairs. (E) Secondary extensions do not shrink beyond forking points. Blue arrows indicate the forking point. (Video S6) Scale bars = 10μm.

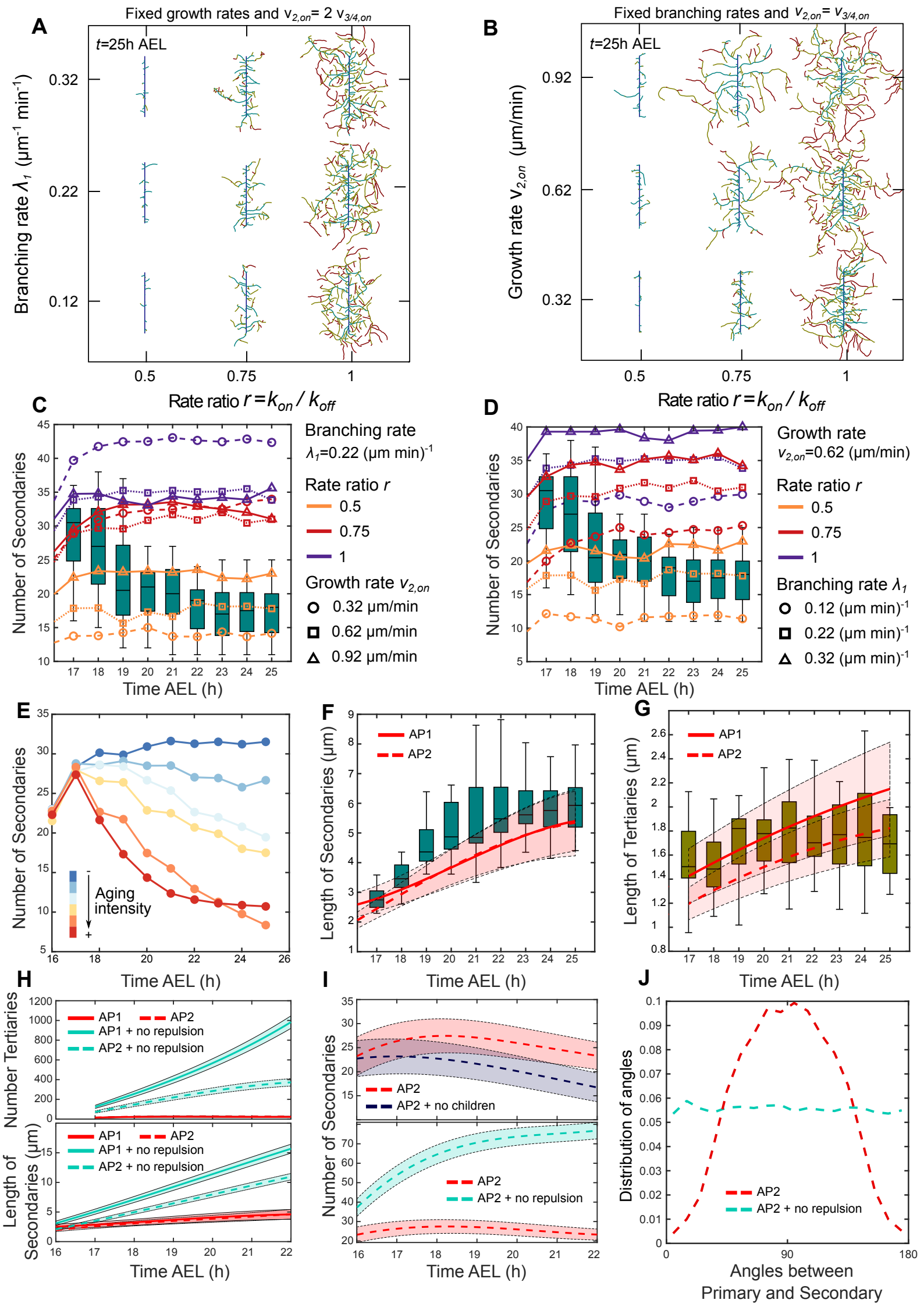
A
Fixed growth rates and $v_{2,on}$= 2 $v_{3/4,on}$
t=25h AEL
Branching rate λ_1 (µm^{-1} min^{-1})
0.32
0.22
0.12
0.5
0.75
1
Rate ratio $r = k_{on} / k_{off}$
B
Fixed branching rates and $v_{2,on}$= $v_{3/4,on}$
t=25h AEL
Growth rate $v_{2,on}$ (µm/min)
0.92
0.62
0.32
0.5
0.75
1
Rate ratio $r = k_{on} / k_{off}$
C
Number of Secondaries
Time AEL (h)
Branching rate
λ_1=0.22 (µm min)$^{-1}$
Rate ratio r
0.5
0.75
1
Growth rate $v_{2,on}$
0.32 µm/min
0.62 µm/min
0.92 µm/min
D
Number of Secondaries
Time AEL (h)
Growth rate
$v_{2,on}$=0.62 (µm/min)
Rate ratio r
0.5
0.75
1
Branching rate λ_1
0.12 (µm min)$^{-1}$
0.22 (µm min)$^{-1}$
0.32 (µm min)$^{-1}$
E
Number of Secondaries
Aging intensity
Time AEL (h)
F
Length of Secondaries (µm)
AP1
AP2
Time AEL (h)
G
Length of Tertiaries (µm)
AP1
AP2
Time AEL (h)
H
Number Tertiaries
AP1
AP2
AP1 + no repulsion
AP2 + no repulsion
Length of Secondaries (µm)
AP1
AP2
AP1 + no repulsion
AP2 + no repulsion
Time AEL (h)
I
Number of Secondaries
AP2
AP2 + no children
AP2
AP2 + no repulsion
Time AEL (h)
J
Distribution of angles
AP2
AP2 + no repulsion
Angles between Primary and Secondary

Figure S3. A computational model for dendrite morphogenesis. Related to Figure 4 and Table 1.

(A) Dendrite morphologies at 25h AEL for the ratio of spontaneous switching rates $r = k_{on}/k_{off}$ vs branching rate of secondary branches $\lambda_{2,on}$ (B) Dendrite morphologies at 25h AEL for ratio of spontaneous switching rates $r = k_{on}/k_{off}$ vs growth rate of secondary branches $v_{2,on}$. The growth rates of tertiary and quaternary branches are given by $v_{2,on} = v_{3/4,on}$ the values of the other computational parameters for (A) and (B) are fixed and detailed in Table 1, Option 1. (C) and (D) Number of secondary branches over time corresponding to (A) and Figure 4C. In both figures, the growth rates for tertiary and quaternary branches are given by $v_{3/4,on} = v_{2,on}/2$ and the other computational values are fixed and given by Table 1, Option 1. (E) Number of secondary branches over time from simulations with identical parameter values but and different aging protocols. (F) Mean length of secondary branches (G) Mean length of tertiary branches over time. For (F) and (G) red lines represent simulations with the two aging protocols AP1 (continuous line) and AP2 (dashed line) and boxplots represent experimental data. (H) Top: Number of Tertiary branches over time for simulations with (red) and without (green) self-repulsion using aging protocols AP1 (continuous line) and AP2 (dashed line) (Fig. 4 (D) Main Text). Bottom: Mean length of secondary branches over time the computational simulations with (red) and without (green) self-repulsion using aging protocols AP1 (continuous line) and AP2 (dashed line). (I) Top: Number of secondary branches over time for simulations with self-repulsion and child branches (red) and with self-repulsion but no child branches (blue) using AP2 Bottom: Number of secondary branches over time for simulations with (red) and without (green) self-repulsion using AP2. (J) Probability distribution of the angles between primary and secondary branches at 22h AEL. Red and green lines represent simulations with and without self-repulsion, respectively using AP2. The number of simulations for all cases in (C) and (D) and (E) was $N_{sim} = 50$. For all cases in (F), (G), (H), (I) and (J) it was $N_{sim} = 500$. In all figures, simulation lines represent the average value of the simulations and shadows represent the 1σ confidence interval. In addition, a 2-point time-averaging was performed using spline interpolation for lines in (F), (G), (H) and (I). For (E), AP1 in (F) and (G), and AP1 with and without self-repulsion in (H) the initial values of the computational parameters are detailed in Table 1, Option 1. For AP2 in (F) and (G), (H), (I) and (J) the initial values of the computational parameters are detailed in Table 1, Option 2. For each box corresponding to *in vivo* observations, the central line is the median, the box extends vertically between the 25th and 75th percentiles and the whiskers extend to the most extreme data that are not considered outliers.

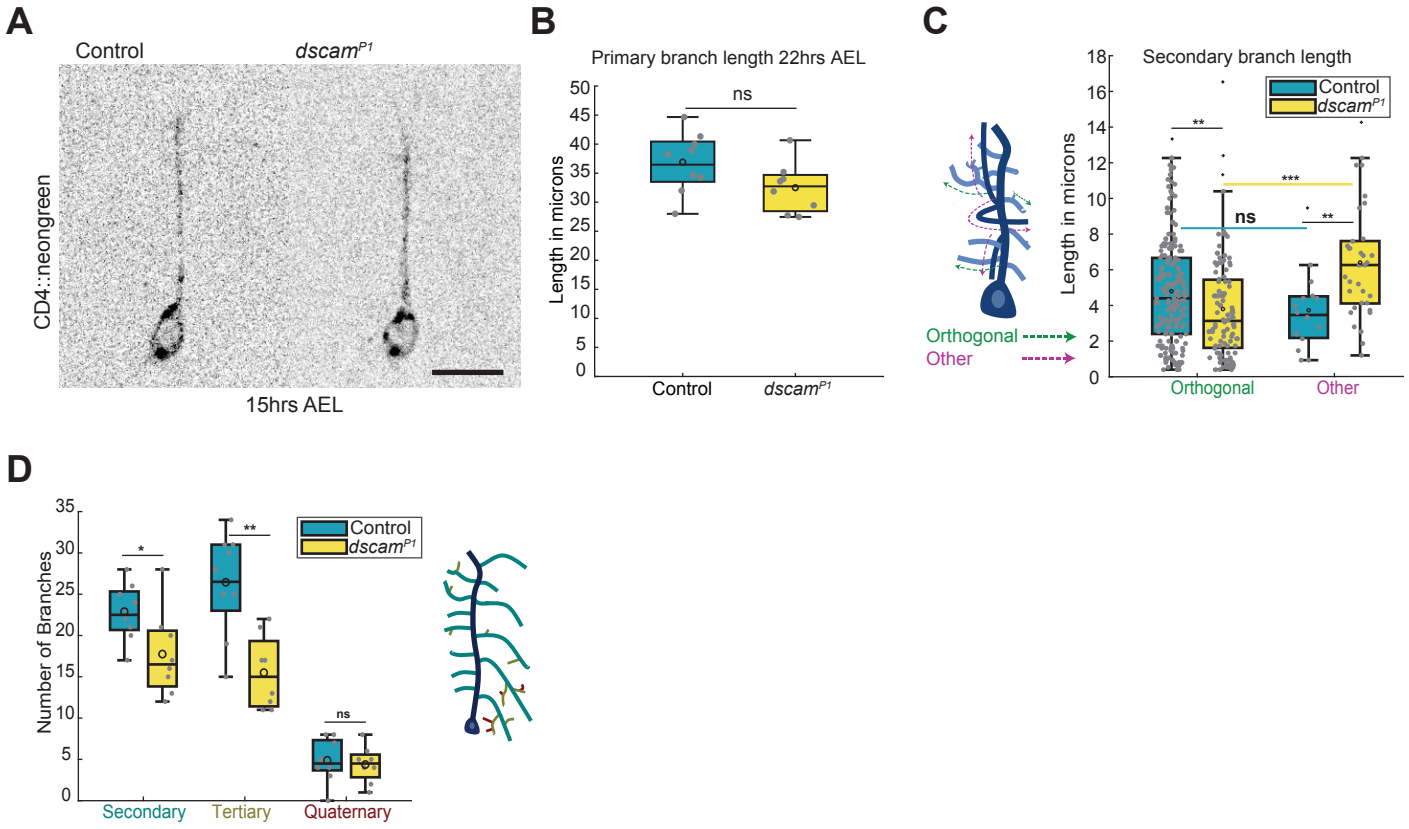

Figure S4. Secondary Branches require Dscam1 to allow a preferential orthogonal stabilization. Related to Figure 5.

(A) Left Panel: Control Class I vpda neurons taken from homozygous embryos of 2- 21gal4/ UAS-mCD4::neongreen. Right Panel: dscamP1 mutant neurons taken from embryos of dscamP1/ΔDscam1;2-21gal4/UAS-mCD4::neongreen. Neurons imaged at ~15h AEL and injected with Ryanodine. (B) Primary branch lengths at ~22h AEL. (C) Schematic: Branches oriented orthogonally (Green arrows) Branches oriented in other directions (magenta arrows). Lengths of Secondary branches oriented orthogonally vs non-orthogonally (other). Orthogonal control (blue) n=188 mutant (yellow) n=107. Other: control (blue) n=15 mutant (yellow) n=34 secondary branches from 9 and 8 neurons respectively. (D) Number of branches at each order of complexity. Schematic: Primary branch (blue) Secondary branches (cyan) Tertiary (brown) Quaternary (red). For (B) and (D) Control (blue) n=9 dscamP1 mutant (yellow) n=8 neurons. For each box, the central line is the median, the 'o' is the mean, the box extends vertically between the 25th and 75th percentiles, the whiskers extend to the most extreme data that are not considered outliers, and the outliers are plotted individually. Statistical significance has been calculated using Mann-Whitney U test. ns, * $p<0.05$; ** $p<0.01$, *** $p<0.001$. All the panels have the same orientation: dorsal at the top, anterior to the left. Scale bars = 10μm.